Robust CFAR Detection of Noise Jamming in Coherent Radars

Anatolii A. Kononov[*]**, Dohyung Kim, Sung-Hyun Choi, and Haksoo Kim**

Abstract—This paper introduces a robust constant false alarm rate (CFAR) method to detect continuous noise jamming in coherent radar systems with a single antenna having no pattern control. The proposed detector is robust to interfering signals such as strong spikes from neighboring radars and returns from targets of interest and is resistant to land, sea, and weather clutter. The detector operates on data vectors extracted from a real-valued Range-Doppler data matrix generated at the output of Doppler processing for each azimuth cell within the entire scanning sector. Each data vector consists of statistically independent range samples associated with one of the specified Doppler bins. These samples are selected from non-overlapping range intervals allocated within the noise-dominant region in the full range coverage to mitigate the effect of clutter on the detector's performance. To perform jamming detection for each cell under test (CUT) in the current antenna scan, the proposed detector uses the CUT-associated data vectors generated in the current antenna scan and CFAR reference data vectors generated in the previous antenna scan. These reference data vectors are extracted from Range-Doppler data matrices associated with reference azimuth cells uniformly distributed within the entire scanning sector. The proposed detector achieves robustness to interfering signals by using a two-step detection algorithm. The first step performs censored video integration (CVI) for the CUT and reference data vectors and individual adaptive CFAR detection in each specified Doppler bin. The detector applies the "m-of-n" detection strategy to a complete set of decisions declared by the individual CFAR detectors in the second step. This strategy provides immunity to the simultaneous presence of interfering signals in the specified Doppler bins. The robustness of the proposed noise jamming detector is verified using Monte-Carlo simulations.

1. INTRODUCTION

One of the effective electronic countermeasures (ECM) techniques commonly used against radar systems is continuous-wave noise jamming [1, Chapter 12] that prevents the detection of targets by raising the receiver noise level. Consequently, the radar detection performance degrades due to the increase in the CFAR threshold that adapts to a higher noise level. Moreover, the presence of noise jamming denies accurate measurements of the target's range and radial velocity.

The most common types of noise jamming techniques are spot noise and barrage noise. A spot noise jammer, which is used when the carrier frequency and the bandwidth of the victim radar are known, has a relatively narrow spectral band and may be effective if its band matches the radar signal bandwidth. If the radar signal bandwidth is unknown to the jammer or the radar changes carrier frequency, the spot jammer loses its effectiveness. The jammer must then employ a wide frequency band that covers the expected radar frequency extent. Such a jammer, called a barrage noise jammer, needs more power than a spot jammer because only some portion of its power lies in the instantaneous bandwidth of the radar receiver. Thus, an effective ECCM technique against noise jamming is varying

radar frequency since it forces the jammer to spread its energy over the broader bandwidth, reducing the power density of jamming if the mean jammer power remains constant at the input of the radar receiver. Frequency changing by the radar can be performed in a manner of frequency agility when radar carrier frequency changes on a pulse-to-pulse basis for non-coherent signal processing modes and a dwell-to-dwell basis when radar echoes received over dwell intervals are coherently processed. Another technique for coherent radars is frequency hopping, when radar changes transmit frequency whenever it detects noise jamming.

The mentioned ECCM techniques are especially suitable for radars we address in the context of this paper: coherent radars with a single antenna having no adaptive pattern control.

To cope with the radar performance degradation caused by noise jamming, a method is required, which would allow to reliably detect the presence of jamming at the specified false alarm rate, i.e., the method has to possess the CFAR property. Also, such a method may be supplemented with a jamming power estimator and, if required, with a direction of arrival estimator. Once the noise jamming is detected and measured, the radar can select the least-jammed carrier frequency (or a set of frequencies) based upon the measured jamming power and implement frequency hopping.

Over the past decades, most published works have addressed antenna-based methods to deny noise jamming attacks; see [1, Chapters 9 and 12], some recent works [2–4], as well as references therein. However, these methods are designed for radar systems with adaptive antenna arrays and, therefore, can not be applied to the radars we address in the context of this paper.

Work [5] introduced a jamming detection method that possesses the CFAR property and can be used in the radars we address herein. This method estimates the statistical distribution of the received signal: an amplitude histogram represents this estimate. Then, it compares the estimated distribution with a reference distribution specified for a predetermined signal model. The result of this comparison is a deviation of the measured distribution from a specified reference distribution. The presence of jamming is determined according to the deviation X: if the deviation exceeds a specified threshold, that is $X \geq X(n, \beta)$, then the presence of jamming is declared. The threshold $X(n, \beta)$ is determined depending on the total number of the received signal samples n that is used for computing the amplitude histogram and on a given probability of false alarm β.

Although the method [5] has the CFAR property, it is not resistant to interfering signals and clutter. Indeed, in the presence of strong clutter returns or interfering signals from neighboring radars, the received signal distribution significantly deviates from the specified reference distribution. Hence, the deviation X computed for the actual received signal may exceed the specified threshold $X(n, \beta)$; therefore, the detection of noise jamming is declared even if no jamming is present.

A robust noise jamming detection method for noncoherent radars with a single nonadaptive antenna was proposed in [6]. This method applies order statistics CFAR to a sequence of azimuthal samples resulted from censored video integration in range for each azimuth resolution cell within the full radar coverage. As shown in [6], the method is reasonably robust to strong spikes and provides reliable noise jamming detection. However, it has no immunity to clutter in the cell under test and CFAR reference data.

The purpose of this paper is to develop a new noise jamming detection method for coherent radars. The new method has to be capable of: 1) detecting, with high probability, the presence of continuous noise jamming; 2) maintaining the specified constant false alarm rate; 3) being robust to strong spikes such as interfering signals from neighboring radars and targets of interest, and 4) being immune to the land, sea and weather clutter.

This paper is organized as follows. Section 2 briefly reviews some basics concepts we use in designing the new method. Section 3 addresses a non-adaptive noise jamming detector (NJD) which assumes that the *receiver thermal noise power is known.* For no interference scenarios, the NJD detector provides the upper detection performance bound for an adaptive noise jamming detector (AJD) we shall introduce in Section 4. We design the AJD detector under the condition that the *receiver thermal noise power is unknown.* Section 3 analyzes the performance of two versions of the NJD detector: the NJD-CVI detector employing the censored video integration (CVI) and the NJD-FVI detector using the full video integration (FVI). This analysis compares their jamming detection performance in a no interference scenario and the robustness of their false alarm performance to strong spikes in the CUT data. Section 4 analyzes the AJD-CVI's detection performance in a no interference scenario and the robustness of its

detection performance to the presence of strong spikes and noise jamming in the CFAR reference data. We also analyze the robustness of the AJD-CVI's false alarm performance to strong spikes in the CUT data. Whenever relevant, we compare the AJD-CVI's performance with that of NJD-CVI. The conclusion is given in Section 5. Appendix A describes an adaptive CFAR method exploited by the AJD-CVI detector.

2. BASIC CONCEPTS

Figure 1 shows a two-dimensional search radar that looks for surface targets in azimuth and range using a fan antenna beam. The radar antenna rotates to scan the entire azimuthal area around the radar (360° coverage in azimuth) and receives returns from some range interval for each azimuth bin, which angular extent is equal to the antenna beamwidth in azimuth.
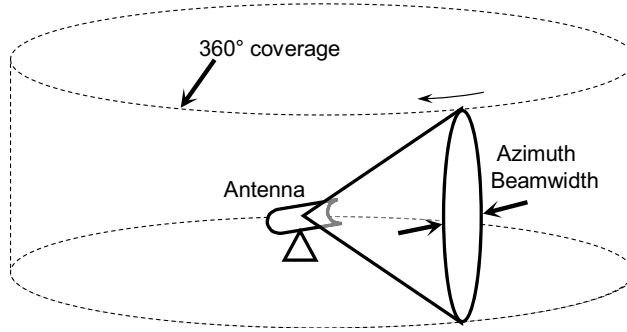

Figure 1. Exemplary scan pattern for surveillance radar.

Signals received by the radar antenna during the dwell time corresponding to each of n_{az} azimuth resolution cells (azimuth bins) are amplified, downconverted, digitized (converted into digital samples), pulse compressed (matched filtering), coherently integrated with Doppler processor followed by a square-law detector, and then collected into an L-by-N Range-Doppler data matrix: L is the number of range bins within the specified range interval, and N is the number of coherently integrated pulses (this is also the number of Doppler bins) within the dwell time interval. Such a Range-Doppler data matrix represents radar-generated information on a specific environmental scene associated with a particular azimuth cell from the full coverage in azimuth.

Figure 2 shows an example of the Range-Doppler data matrix for $L \gg 1$ and $N = 16$, assuming no continuous noise jamming in a particular azimuth bin associated with this data matrix. In addition to the receiver thermal noise, which samples occupy all Range-Doppler bins, this data matrix contains samples representing a specific radar scenario. In this scenario, there are four targets (the target-associated samples appear as black circles at Doppler bins 3, 8, 9, and 11), and extended in range sea clutter mainly concentrated in Doppler bin 9 (zero Doppler), and an extended in range rain clutter concentrated in Doppler bin 5.

The receiver thermal noise is a zero-mean Gaussian random process [7, Chapter 2]. At the input of a square-law detector, the I and Q samples of the thermal noise can be modeled as statistically independent Gaussian random values, which probability density function $w_n(x)$ is given by

$$w_n(x) = \left(\sqrt{2\pi \left(\sigma_n^2/2 \right)} \right)^{-1} \exp \left(-\frac{x^2}{2 \left(\sigma_n^2/2 \right)} \right) \tag{1}$$

where σ_n^2 is the receiver thermal noise power after Doppler processing. The magnitude-squared noise samples at the output of the square-law detector (SLD) are independent exponentially distributed (i.e.d.) random values (r.v.) with the probability density function $p_n(x)$ [7]

$$p_n(x) = \frac{1}{\sigma_n^2} \exp \left(-\frac{x}{\sigma_n^2} \right) \tag{2}$$
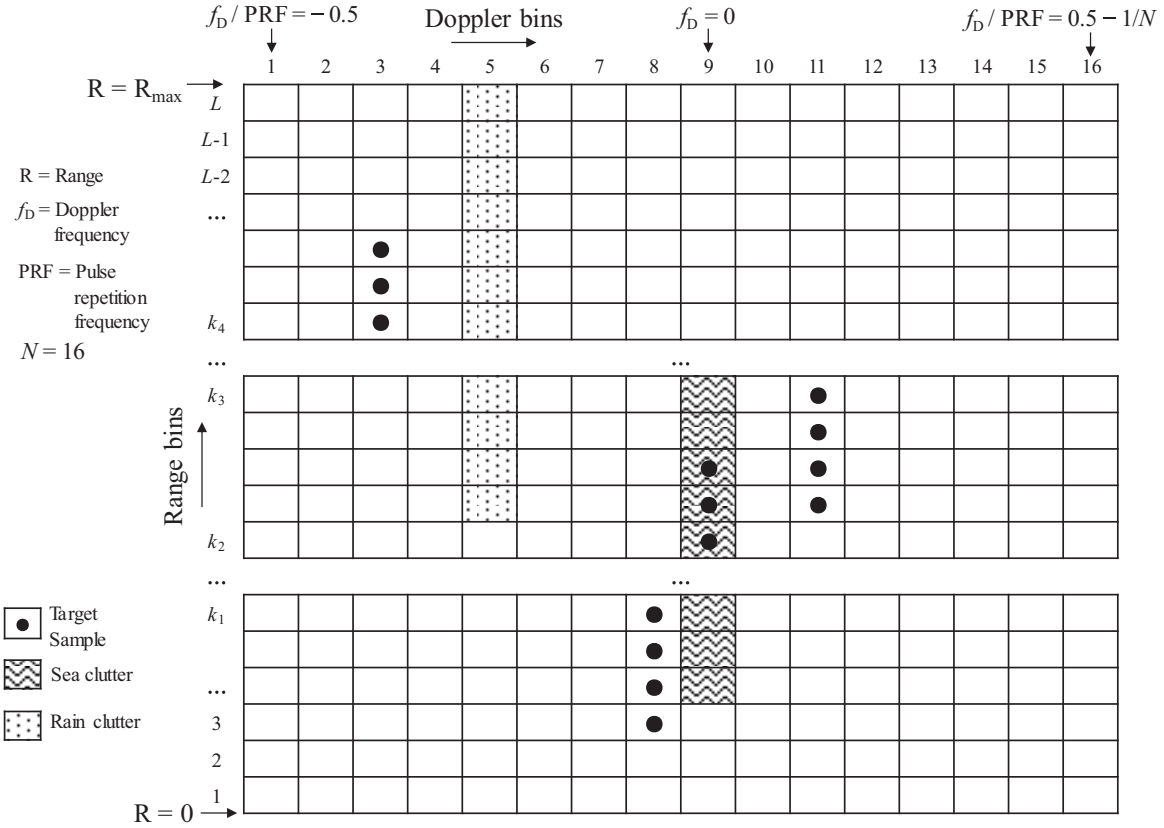
Figure 2. Example of Range-Doppler data matrix.

The model for noise jamming is also a zero-mean white Gaussian process statistically independent of the receiver thermal noise. Therefore, when the noise jamming with power σ_j^2 is present, the total noise power increases to $\sigma_n^2 + \sigma_j^2$ and the resulting I and Q samples at the input of the SLD are also independent Gaussian values, which probability density function is

$$w_{n+j}(x) = \left(\sqrt{2\pi \left([\sigma_n^2 + \sigma_j^2]/2 \right)} \right)^{-1} \exp\left(-\frac{x^2}{2 \left([\sigma_n^2 + \sigma_j^2]/2 \right)} \right) \tag{3}$$

Thus, in the presence of noise jamming, the magnitude-squared noise samples at the SLD output are i.e.d.r.v., which probability density function is

$$p_{n+j}(x) = \frac{1}{\sigma_n^2 + \sigma_j^2} \exp\left(-\frac{x}{\sigma_n^2 + \sigma_j^2} \right) \tag{4}$$

or

$$p_{n+j}(x) = \frac{1}{\sigma_n^2(1 + \text{JNR})} \exp\left(-\frac{x}{\sigma_n^2(1 + \text{JNR})} \right) \tag{5}$$

where $\text{JNR} = \sigma_j^2/\sigma_n^2$ is the jamming-to-noise ratio (JNR).

The method proposed in this paper is robust in the sense of immunity to strong spiky signals (such as asynchronous spikes from neighboring radars), returns from targets of interest, and the land, sea, and weather clutter. For the NJD and AJD detector, the term "robust" indicates its ability to maintain the overall probability of false alarm P_{FA} at some low level despite the presence of one or more strong spikes and clutter in the CUT. For the AJD detector, this term also reflects its ability to maintain

reliable detection performance (overall probability of detection P_D) in the presence of strong spikes, noise jamming, and clutter in CFAR reference data.

To provide robustness to strong spikes, the methods proposed in this paper employ the so-called censored video integration (CVI) [8, 9]. As shown in [8], CVI is immune to spikes yet suffers a small loss relative to the full video integration (FVI) that sums all Q samples in each vector representing data associated with an azimuth CUT or with CFAR reference data. Moreover, CVI provides the minimal SNR loss relative to FVI among all robust integration techniques analyzed in [9].

The CVI-integrator works as follows. Let z_1, z_2, ..., z_Q be an initial set of samples in one of the data vectors. First, it sorts the samples according to their magnitudes to obtain the ordered sequence of samples $x_1 \le x_2 \le ... \le x_Q$. After sorting, it integrates the lowest K_c samples: however, this is not a simple summation. Whereas each of the lowest $K_c - 1$ ordered samples is given a unit weight, the K_c-th ordered sample is given a weight $Q - K_c + 1$. Therefore, the CVI-integrator output is

$$Y = (Q - K_c) x_{K_c} + \sum_{i=1}^{K_c} x_i \qquad (6)$$

where K_c is the highest order used in the censoring, $K_c \in \{1, 2, ..., Q\}$. It is clear that CVI provides immunity against $Q - K_c$ strong spikes. Additionally, it possesses the following important property. As has been proven in [10, 11], when z_1, z_2, ..., z_Q are i.e.d.r.v. the statistical distribution of Y in Eq. (6) is the same as that for the sum of only K_c i.e.d.r.v. without sorting. We use this property to derive the detection performance for noise jamming detectors with CVI.

3. NONADAPTIVE NOISE JAMMING DETECTOR

3.1. Block Diagram

In this section, we assume that the receiver thermal noise power σ_n^2 is known. The noise jamming detection algorithm designed under this assumption is a non-adaptive jamming detector (NJD). For no interference scenarios, the NJD detector achieves ultimate jamming detection performance that serves as a reference for an adaptive jamming detector (AJD) that we shall consider in Section 4. Figure 3 shows a block diagram of NJD with CVI (NJD-CVI) as a sequence of operations implemented by computing units CU1, ..., CU5.

CU1 extracts from the input data matrix $\mathbf{B}$ (L-by-N matrix representing a specific radar scene for each particular azimuth cell in radar coverage) a set of vectors $\mathbf{v}_i$, $i = 1, 2, ..., D$

$$\mathbf{v}_1 = [v_{11}, v_{21}, ..., v_{Q1}]^T, \quad \mathbf{v}_2 = [v_{12}, v_{22}, ..., v_{Q2}]^T, \quad ..., \quad \mathbf{v}_D = [v_{1D}, v_{2D}, ..., v_{QD}]^T \qquad (7)$$

where Q is the number of the range bin indices for each of the specified Doppler bin indices n_1, n_2, ..., n_D, and the symbol ^{T} denotes the transposition.

CU2 sorts the samples in each vector $\mathbf{v}_i$ in ascending order to obtain the corresponding sets $\mathbf{x}_i$ of ordered samples

$$\mathbf{x}_i: \quad x_{1i} \le x_{2i} \le ... \le x_{Qi}, \quad i = 1, 2, ..., D \qquad (8)$$

CU3 performs CVI for each $\mathbf{x}_i$, $i = 1, 2, ..., D$ according to Eq. (6)

$$Y_i = (Q - K_c) x_{K_c i} + \sum_{j=1}^{K_c} x_{ji}, \quad i = 1, 2, ..., D \qquad (9)$$

where K_c is the censoring rank, $K_c \in \{1, 2, ..., Q\}$.

CU4 implements the following operations:

a) Perform individual detections for each of the specified Doppler bins using the following sequence of statistical hypothesis tests

$$Y_i \underset{H_o}{\overset{H_1}{\gtrless}} T = \alpha \sigma_n^2, \quad i = 1, 2, ..., D \qquad (10)$$

where T is the detection threshold, and α is the threshold multiplier precomputed for the specified individual probability of false alarm P_{fa}, which is the same for all individual detections; H_o and H_1 respectively stand for the null hypothesis (no noise jamming) and the alternative hypothesis (noise jamming is present).

Range-Doppler Data Matrix **B**

Matrix $\mathbf{B} = [b_{mn}]$, $m = 1, \ldots, L$; $n = 1,\ldots,N$ is L-by-N real-valued Range-Doppler data matrix representing a specific radar scene for each particular azimuth cell in turn

CU1

Generate Q-by-1 vectors $\mathbf{v}_i$, $i = 1, 2, .., D$ for the specified Doppler bin indices $n_1, n_2, .., n_D$

CU2

Sort the samples in each vector $\mathbf{v}_i$ in ascending order to obtain the corresponding sets $\mathbf{x}_i$ ($i = 1, .., D$) of ordered samples
$\mathbf{x}_i$: $x_{1i} \leq x_{2i} \leq \ldots \leq x_{Qi}$

K_c is the censoring rank, $K_c \in \{1,2,..,Q-1\}$

CU3

Perform censored video integration (CVI) for each $\mathbf{x}_i$, that is, compute the following scalar values
$Y_i = (Q - K_c)x_{K_ci} + \sum_{j=1}^{K_c} x_{ji}$, $i = 1,2,..,D$

$\mathbf{v}_1 = \left[v_{11}, v_{21}, \ldots, v_{Q1}\right]^{\mathrm{T}}$
$\mathbf{v}_2 = \left[v_{12}, v_{22}, \ldots, v_{Q2}\right]^{\mathrm{T}}$
$\cdots$
$\mathbf{v}_D = \left[v_{1D}, v_{2D}, \ldots, v_{QD}\right]^{\mathrm{T}}$

Q is the number of the specified range bin indices for each of the D specified Doppler bin indices $n_1, n_2, \ldots, n_D$

α is the threshold multiplier precomputed for the individual probability of false alarm P_{fa} which relates to individual detections for each of the specified Doppler bins

σ_n^2 is the receiver thermal noise power (assumed to be known)

CU4

Perform individual detections of noise jamming using the rule
$Y_i \gtrless T$, $T = \alpha\sigma_n^2$, $i = 1, \ldots, D$
and count the number of cases when Y_i exceeds the threshold T. Let this number be N_d

CU5

Perform final noise jamming detection using the principle of binary integration for the individual detections:
if $N_d \geq D_{\mathrm{T}}$ jamming is present, otherwise no jamming
(D_{T} is the threshold for the number of detections)

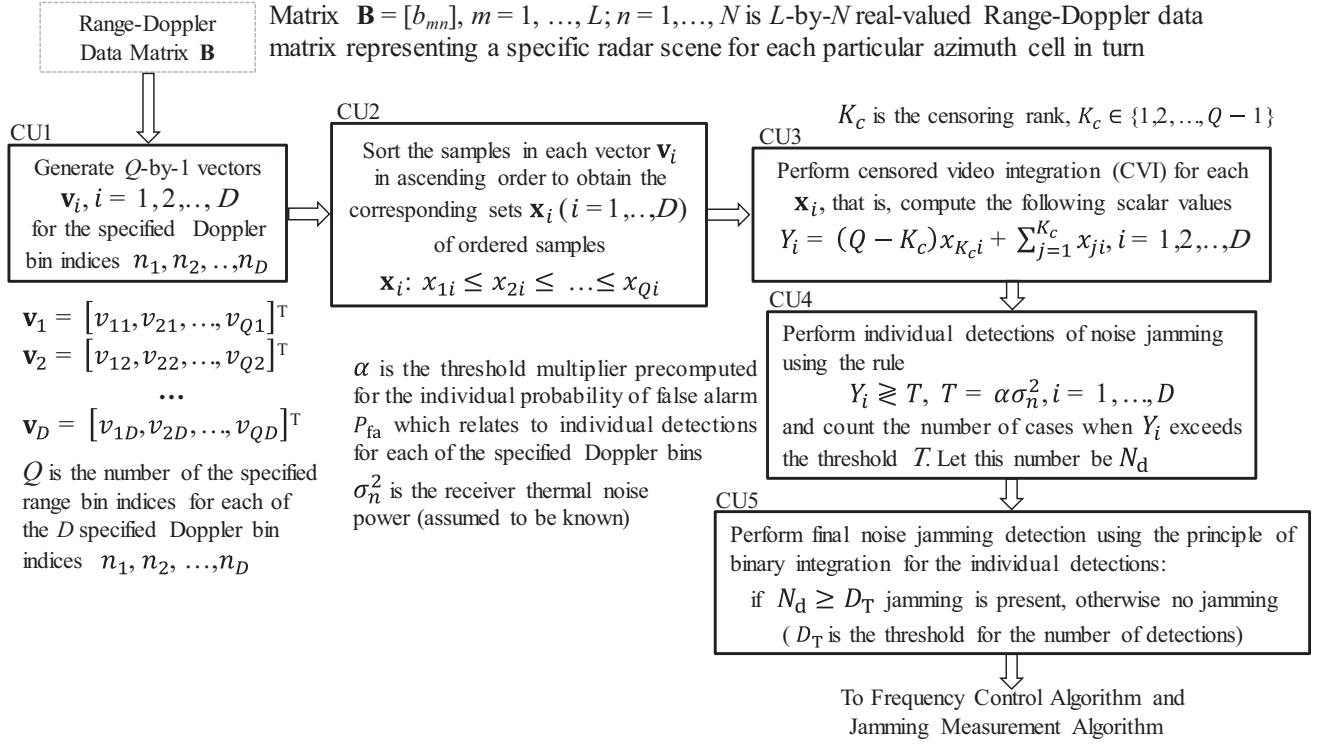To Frequency Control Algorithm and Jamming Measurement Algorithm

Figure 3. Nonadaptive noise jamming detector with CVI (known receiver noise power).

b) Count the number of detections N_d (the number of cases when Y_i, $i = 1, 2, ..., D$ exceeds the fixed precomputed detection threshold T) out of the total number of possible detections D, and accumulates the vector of detected Y_i samples: $[Y_{i_1}, Y_{i_2}, ..., Y_{i_{N_d}}]$, where $i_1, i_2, ..., i_{N_d}$ are the indices of those Doppler bins at which noise jamming detection occurred.

CU5 implements final noise jamming detection using the m-out-of-n detection strategy

$$\text{if } N_d \geq D_T \text{ noise jamming is present, otherwise no jamming} \tag{11}$$

where D_T is the integer threshold ($0 < D_T \leq D$) for the number of individual detections.

Whenever CU5 declares the presence of noise jamming (decides that hypothesis H_1 is true), it sends a warning signal to the so-called Frequency Control Algorithm (FCA). CU5 also sends a set of detected samples $[Y_{i_1}, Y_{i_2}, ..., Y_{i_{N_d}}]$ to the Jamming Measurement Algorithm (JMA) that estimates the average noise jamming power. FCA decides what a new carrier frequency (or a new set of carrier frequencies) from a set of permissible radio frequencies (RFs) is the best choice for current radar operations. One of the reasonable criteria for the best choice is to select that RF (or a set of RFs), which is jamming-free; otherwise, if all permissible RFs are currently affected by noise jamming, that one, for which the estimated average jamming-to-noise ratio (JNR) is minimal. These estimates may be stored in a look-up table available to FCA.

3.2. Data Extraction from a Range-Doppler Matrix

Figures 4(a) and 4(b) illustrate some possible arrangements for selecting the range-Doppler samples from the input matrix $\mathbf{B} = [b_{mn}]$ ($m = 1, ..., L$; $n = 1, ..., N$), which are to be used for generating the set of the vectors $\mathbf{v}_i$ given by Eq. (7). In selecting these samples, the primary goal is to ensure that they contain as low as possible clutter power due to sea, land, and weather clutter.

Typically, the clutter intensity concentrates in the vicinity of a fixed Doppler frequency. Therefore, for a given number of coherently processed pulses N, the number of Doppler bins D ($D \geq 3$) and their separations in the Doppler dimension should be chosen to ensure a low clutter power leakage

Input Range-Doppler data matrix $\mathbf{B}$

Q range samples taken at specified Doppler bins

$n_1, n_2, \ldots, n_D$

to generate the vectors

$\mathbf{v}_i, i = 1, 2, \ldots, D$

In this example, $D = 5$ and $n_1 = 1, n_2 = 4, n_3 = 7,$ $n_4 = 11, n_5 = 14$

Vectors $\mathbf{v}_i = \left[v_{1i}\ v_{2i}\ \ldots v_{Qi}\right]^{\mathrm{T}}, i = 1, \ldots, D$ are generated from the entries in the input Range-Doppler data matrix $\mathbf{B} = \left[b_{mn}\right]$ as follows:

$$\mathbf{v}_i = \left[b_{m_{1i}n_i}, b_{m_{2i}n_i}, \ldots, b_{m_{Qi}n_i}\right]^{\mathrm{T}}$$

where $m_{1i} < m_{2i} < \ldots < m_{Qi}$ are the range bin indices specified for a given Doppler bin index n_i, $i = 1, \ldots, D$

(a)

Input Range-Doppler data matrix $\mathbf{B}$

Q range samples taken at specified Doppler bins

$n_1, n_2, \ldots, n_D$

to generate the vectors

$\mathbf{v}_i, i = 1, 2, \ldots, D$

In this example, $D = 4$ and $n_1 = 1, n_2 = 5, n_3 = 9,$ $n_4 = 13$
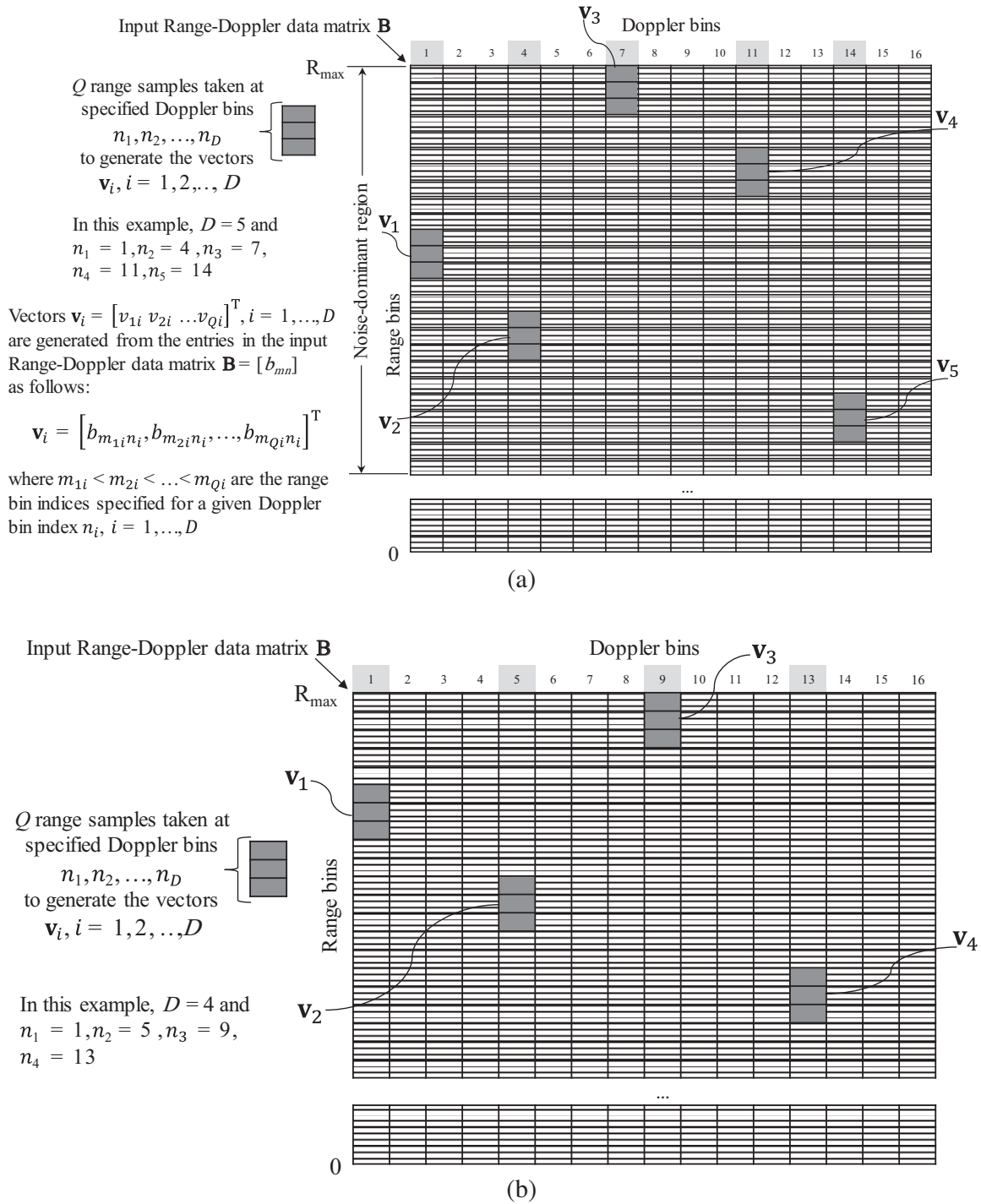
(b)

Figure 4. Some possible arrangements for extracting data from a Range-Doppler data matrix.

between the selected Doppler bins. To provide a low power of the sea, land, and weather clutter in the selected Range-Doppler samples, we suggest arranging the corresponding range intervals within the noise-dominant range region and as close as possible to the maximum range point $R_{\max}$. The noise-dominant range region is that part of the full range coverage, for which the clutter-to-noise ratio (CNR) does not exceed unity (CNR < 1) for all possible types of clutter the radar is designed to operate in. To guarantee the mutual statistical independence of the said Range-Doppler samples, these samples for

each vector $\mathbf{v}_i$ $(i = 1, 2, ..., D)$ should be selected from non-overlapping range intervals. If possible, there should be as wide as possible gaps between these range intervals.

As follows from Eq. (9), to compute the scalar Y_i for each $\mathbf{x}_i$, CVI discard the $Q - K_c$ largest samples $x_{(K_c+1)i}, x_{(K_c+2)i}, ..., x_{Qi}$ (censoring procedure) and uses only the lowest K_c samples $x_{1i}, x_{2i}, ..., x_{K_ci}$. It is well known [8, 9, 11] that discarding the $Q - K_c$ largest samples ensures the robustness of individual detections given by Eq. (10) to strong spikes if their number does not exceed $Q - K_c$. Such strong spikes can appear when several radars operate nearby or due to targets of interest: returns from these targets act as interfering signals for noise jamming detectors. However, CVI does not provide immunity to range-extended clutter that may corrupt all samples in the vector $\mathbf{v}_i$.

The m-out-of-n detection strategy (Figure 3, CU5) improves the overall robustness of the NJD-CVI detector by providing immunity to interfering signals, including clutter, that may simultaneously present in several Doppler bins. Indeed, if individual detectors have declared N_d detections due to the presence of strong spikes or sea, land or weather clutter, the NJD-CVI detector will maintain the overall robustness as long as the condition $N_d < D_T$ is met. In designing radar systems, radar engineers have the freedom to choose the parameters Q, K_c, D, and D_T. One can choose to have the following event highly improbable to occur. This event is the presence of more than $Q - K_c$ strong interfering signals simultaneously in D_T or more well-separated Doppler bins out of all D Doppler bins for a particular azimuth cell, i.e., within a limited angular extent on the order of antenna beamwidth. For example, setting $Q = 24$, $K_c = 18$, $D = 5$, and $D_T = 3$ may be a practically reasonable choice. On the other hand, when the noise jamming is present in the CUT-associated azimuth cell, the total noise power level increases simultaneously in all Range-Doppler cells (in all entries of the CUT-associated Range-Doppler data matrix $\mathbf{B}$). The overall noise power increase provides favorable conditions for detecting continuous noise jamming, especially when JNR $\gg 1$.

3.3. NJD Performance Analysis

3.3.1. No Interference in Cell under Test

The overall probability of detection P_D for NJD is given by the known expression for the m-of-n strategy [7] as the probability of at least $m = D_T$ detections out of all $n = D$ detections

$$P_D = P_D\left(D_T, D\right) = \sum_{k=D_T}^{D} \frac{D!}{k!\left(D-k\right)!}\left(P_d\right)^k\left(1 - P_d\right)^{D-k} \tag{12}$$

where P_d is the individual probability of detection for each of the individual detectors in Eq. (10).

Similarly, the overall probability of false alarm P_{FA} (at least D_T false detections out of all D detections when no noise jamming is present) is given by

$$P_{\text{FA}} = P_{\text{FA}}\left(D_T, D\right) = \sum_{k=D_T}^{D} \frac{D!}{k!\left(D-k\right)!}\left(P_{\text{fa}}\right)^k\left(1 - P_{\text{fa}}\right)^{D-k} \tag{13}$$

where P_{fa} is the individual probability of false alarm for each detector in Eq. (10).

To derive the equation for the individual probability of detection P_d, we refer to [9, 10]. As has been proven therein, when the elements in vectors $\mathbf{v}_i = [v_{1i}, v_{2i}, ..., v_{Qi}]$, $i = 1, ..., D$ are i.e.d.r.v.then the statistical distribution of the corresponding random values Y_i, $i = 1, ..., D$ in Eq. (9) is the same as that for the sum of only K_c i.e.d.r.v. without sorting. Thus, the random variables Y_i, $i = 1, ..., D$ are independent, and each of them obeys a gamma distribution with a shape parameter K_c and scale parameter θ. The probability density function (PDF) $p_Y(y)$ and the cumulative distribution function (CDF) $P_Y(y)$ for this distribution are, respectively

$$p_Y(y) = \frac{1}{(K_c - 1)!} \frac{1}{\theta^{K_c}} y^{K_c-1} e^{-\frac{y}{\theta}}, \tag{14}$$

$$P_Y(y) = 1 - e^{-\frac{y}{\theta}} \sum_{i=0}^{K_c-1} \frac{(y/\theta)^i}{i!}, \tag{15}$$

where the parameter θ is given by

$$\theta = \begin{cases} \sigma_n^2, & \text{if noise jamming is not present} \\ \sigma_n^2\left(1 + \text{JNR}\right), & \text{if noise jamming is present} \end{cases} \tag{16}$$

In the presence of noise jamming, the individual detection at the i-th specified Doppler bin takes place when Y_i $(i = 1, 2, ..., D)$ exceeds a predetermined threshold $T = \alpha \sigma_n^2$. The individual probability of detection is therefore

$$P_D = 1 - P_Y(T), \tag{17}$$

which gives taking into account Eq. (15)

$$P_d = e^{-\frac{T}{\sigma_n^2(1+\text{JNR})}} \sum_{k=0}^{K_c-1} \frac{\left(\frac{T}{\sigma_n^2(1+\text{JNR})}\right)^k}{k!} \tag{18}$$

Noting that $T = \alpha \sigma_n^2$, we get

$$P_d = e^{-\frac{\alpha}{1+\text{JNR}}} \sum_{k=0}^{K_c-1} \frac{\left(\frac{\alpha}{1+\text{JNR}}\right)^k}{k!} \tag{19}$$

The individual probability of false alarm P_{fa} is readily obtained from Eq. (19) at $\text{JNR} = 0$

$$P_{\text{fa}} = e^{-\alpha} \sum_{k=0}^{K_c-1} \frac{(\alpha)^k}{k!} \tag{20}$$

For a given P_{fa}, the corresponding threshold multiplier α (this multiplier is equal to the threshold value T normalized to σ_n^2) is computed iteratively from Eq. (20).

As has been proved in [10], the detection rule given by Eq. (10) is the best statistical test that uses first K_c ordered samples (from a total set of Q i.e.d.r.v.) to detect white Gaussian noise. The term "best" means, according to the usual Neyman-Pearson terminology, a test which ensures the maximum detection probability P_d among all statistical tests having a fixed probability of false alarm, which is equal to a given individual P_{fa}. Thus, for any fixed P_{fa} NJD provides the ultimate detection performance when the first K_c ordered samples from an entire set of Q i.e.d.r.v. are used.

In terms of detection performance, full video integration (FVI) is the most efficient among all the noncoherent integration methods studied in [9]. Therefore, it is reasonable to compare the detection performance of the NJD-CVI detector against that of the NJD-FVI detector.

The FVI-integrator computes the sum of all samples z_1, z_2, ..., z_Q

$$Y = \sum_{i=1}^{Q} z_i \tag{21}$$

If these samples are i.e.d.r.v., the random value Y obeys a gamma distribution with a shape parameter Q and scale parameter θ. Therefore, the expressions for the PDF and CDF of Y in Eq. (21) directly follow from Eqs. (14) and (15), respectively, after substituting K_c with Q. If the individual detector in Eq. (10) employs FVI instead of CVI, then one can directly obtain from Eqs. (19) and (20) the individual probability of detection and false alarm for the NJD-FVI detector as

$$P_d = e^{-\frac{\alpha}{1+\text{JNR}}} \sum_{k=0}^{Q-1} \frac{\left(\frac{\alpha}{1+\text{JNR}}\right)^k}{k!} \tag{22}$$

$$P_{\text{fa}} = e^{-\alpha} \sum_{k=0}^{Q-1} \frac{(\alpha)^k}{k!} \tag{23}$$

respectively, where the constant α is computed iteratively from Eq. (23) given P_{fa}.

Figure 5 compares the receiver operating characteristic (ROC) of NJD-CVI and that of NJD-FVI in the absence of interference; the ROC plots (P_D vs. JNR) were computed for $P_{\text{fa}} = 10^{-3}$, $Q = 24$, $K_c = 18$, $D = 5$, and $D_T = 3$. The threshold multiplier for NJD-CVI $\alpha = 33.9925842$ and that for NJD-FVI $\alpha = 42.0185661$ were calculated iteratively from Eqs. (20) and (23), respectively. For both the NJD-CVI and NJD-FVI detectors, the overall probability of false alarm $P_{\text{FA}} = 9.9850057 \times 10^{-9}$ was computed from Eq. (13). The individual probability of detection P_d was computed from Eq. (19) for NJD-CVI and from Eq. (22) for NJD-FVI. The ROC curves were computed using Eq. (12) for both NJD-CVI and NJD-FVI. From Figure 5, one can see that the penalty for the robustness of NJD-CVI
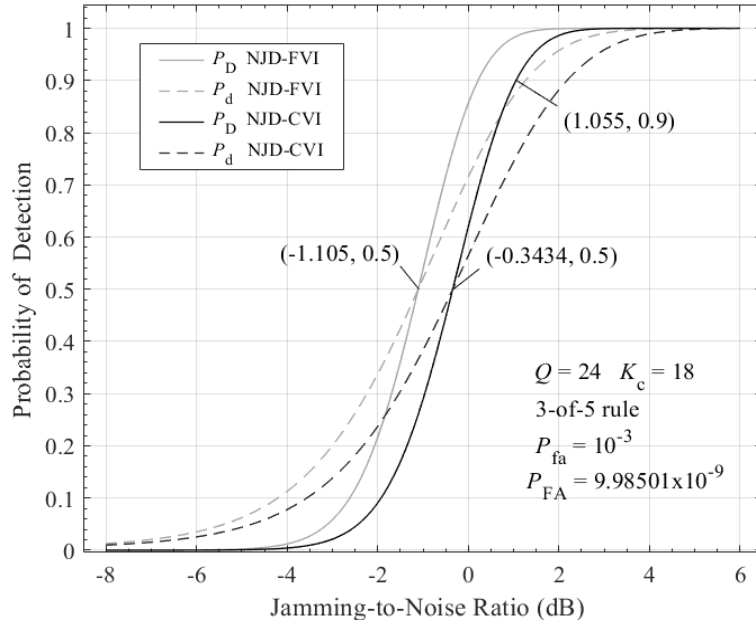
Figure 5. Receiver operating characteristics of NJD-CVI and NJD-FVI.

is an added integration loss in the JNR relative to NJD-FVI: this loss is about $0.76\,\mathrm{dB}$ at $P_D = 0.5$. This relatively small JNR loss explains the NJD-CVI's capability to provide reliable noise jamming detection. Indeed, for such a low overall probability of false alarm ($P_{\mathrm{FA}} \approx 10^{-8}$), NJD-CVI ensures a high overall probability of detection ($P_D \geq 0.9$) starting from JNR $= 1\,\mathrm{dB}$.

It is noteworthy that in NJD-CVI, one has the freedom to choose the parameter K_c ($K_c \leq Q$) that defines the number of samples to be integrated. Figure 6 illustrates how the added JNR loss drops as K_c approaches Q. The price paid for this decrease is a corresponding degradation in robustness to strong spikes.
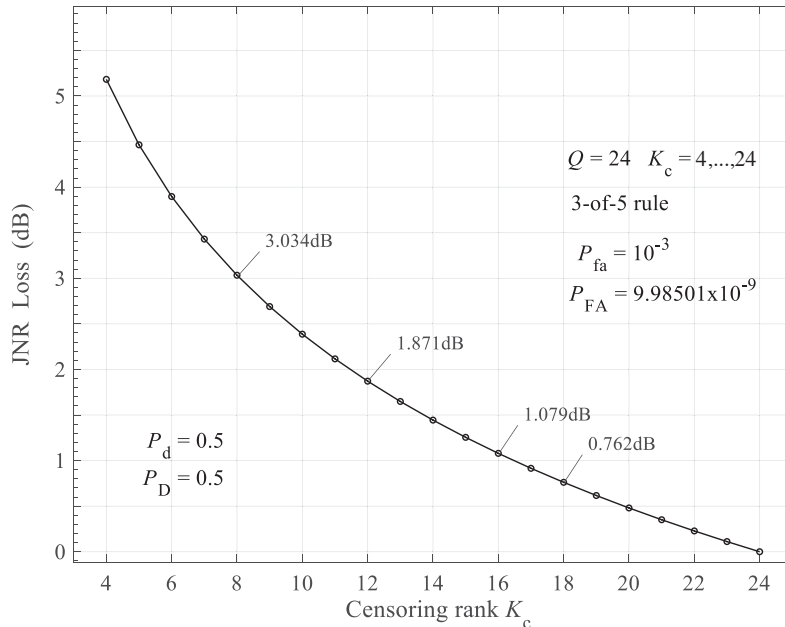

Figure 6. JNR loss for NJD-CVI relative to NJD-FVI versus the censoring rank K_c.

3.3.2. NJD False Alarm Performance in the Presence of Strong Spikes

For detectors of noise jamming, the critical consequence caused by strong spikes in the CUT is increasing the probability of false alarm. A principal drawback of FVI is its essential sensitivity to strong spiky interference. As follows from Eq. (21), the presence of even a single infinitely strong spike in a data vector associated with any Doppler bin will inevitably result in a false alarm. This false alarm occurs because the FVI's output sum Y will exceed the threshold with probability unity even if the remaining samples represent the receiver thermal noise.

In the case of CVI, the $n_{\rm sp}$ infinitely strong spikes in the data vector $\mathbf{v}_i$ $(i = 1, ..., D)$ associated with the n_i-th Doppler bin (see Figure 3) will always occupy the top $n_{\rm sp}$ ranks in the corresponding sorted data vector $\mathbf{x}_i$. Hence, the number of effective samples reduces from Q to $Q_{\rm sp} = Q - n_{\rm sp}$. The distributions of order statistics in Eq. (8) depends on the number of effective samples Q_e. The k-th rank sample $(k \geq 1)$ out of $Q_e = Q_{\rm sp} < Q$ independent identically distributed (i.i.d.) samples is *statistically higher* than the k-th rank sample out of Q i.i.d. samples. The term *statistically higher* means the following relationship between the corresponding PDFs

$$p_{k:Q_{\rm sp}}(x) > p_{k:Q}(x), \ x \geq T, \ Q_{\rm sp} < Q \tag{24}$$

where $p_{k:Q_e}(x)$ stands for the PDF of the k-th order statistic out of Q_e (i.i.d.) samples and T is the threshold corresponding to a sufficiently low probability of false alarm $P_{\rm fa}$.

Since for $Q_e = Q_{\rm sp}$, the PDFs for all order statistics involved in Eq. (8) are not identical to the corresponding PDFs for $Q_e = Q$, a new PDF of the weighted sum Y_i in Eq. (9) is not equal to the PDF of K_c unsorted i.e.d. samples [see Eq. (14)], in the absence of spikes in the corresponding CUT data vector $\mathbf{v}_i$. Eq. (24) suggests that the new PDF exceeds that in Eq. (14): $p_{Y_i}(x) > p_Y(x), \ x \geq T$. Thus, the presence of strong spikes even in one of the CUT data vectors inevitably increases the individual and overall probability of false alarm.

This subsection analyzes the increase in the overall probability of false alarm $P_{\rm FA}$ due to the presence of strong spikes in the CUT under the condition that the threshold multiplier α is set to yield the nominal $P_{\rm fa}$ (and, accordingly, $P_{\rm FA}$) assuming no interferences. To compute α, we used Eq. (20) for NJD-CVI, and Eq. (23) for NJD-FVI.

To evaluate the NJD-CVI's robustness, we resorted to the Monte-Carlo simulation. This simulation was carried out for a single individual detector in Eq. (10) associated with one of the Doppler bins. In this simulation, the strong spikes were specified as infinitely large constants. The simulation results are the estimates of the conditional individual probability of false alarm $P_{\rm fa}(n_{\rm sp}|1)$. This probability is conditioned on the number of strong spikes $n_{\rm sp}$ present in the data vector $\mathbf{v}_1$ associated with a single Doppler bin n_1. For brevity, we will refer to $n_{\rm sp}$ as "the number of spikes per one Doppler bin." Let these estimates be

$$\hat{P}_{\rm fa}(n_{\rm sp}|1), n_{\rm sp} = 0, 1, 2, ..., n_{sp}^{\rm max} \tag{25}$$

where $n_{\rm sp}^{\rm max}$ is the maximum number of spikes per one Doppler bin and $\hat{P}_{\rm fa}(n_{\rm sp} = 0|1) = P_{\rm fa}$ (nominal value).

To estimate the unconditional individual probability of false alarm for a single Doppler bin, we assume that the number of strong spikes per one Dopper bin is a random value s_k, $k = 0, 1, ..., n_{sp}^{\rm max}$, uniformly distributed over the corresponding k-th set $\mathcal{S}_k$ of integers: $s_k \sim U : \mathcal{S}_k = \{0, 1, ..., k\}$. Averaging the estimates from Eq. (25) over the set $\mathcal{S}_k$ yields the corresponding estimates of the unconditional individual probability of false alarm $P_{\rm fa:1}(n_{\rm sp}^{\rm max})$ for a single Doppler bin as

$$\hat{P}_{\rm fa:1}\left(n_{\rm sp}^{\rm max}\right) = \left(\frac{1}{q+1}\right) \sum\nolimits_{n_{\rm sp}=0}^{q} \hat{P}_{\rm fa}(n_{\rm sp}|1), \ q = 0, 1, ..., n_{sp}^{\rm max} \tag{26}$$

Having obtained the estimates in Eq. (26), one can compute the corresponding estimates of the overall probability of false alarm $P_{\rm FA}(n_{\rm sp}^{\rm max}|d_{\rm sp})$ conditioned on $d_{\rm sp}$, where $d_{\rm sp} \in \{1, ..., D\}$ is the number of vectors $\mathbf{v}_i$, $i \in \{1, 2, ..., D\}$ affected by strong spikes. For brevity, we refer to the parameter $d_{\rm sp}$ as the number of spiky Doppler bins. For the "D_T-of-D" overall detection strategy with $D_T = 3$, these estimates are given by

$$\hat{P}_{\rm FA}(n_{\rm sp}^{\rm max}|d_{\rm sp}) = 1 - \left[\hat{\mathcal{P}}_0 + \hat{\mathcal{P}}_1 + \hat{\mathcal{P}}_2\right]$$
$$d_{\rm sp} \in \{1, ..., D\} \tag{27}$$

where $\hat{\mathcal{P}}_r$, $r \in \{0, 1, 2\}$ is the estimate of the probability of exactly r detections out of all D possible detections. Since the false alarms for any subset of Doppler bins are mutually independent events, these estimates are given by

$$\hat{\mathcal{P}}_0 = \Pi_{i=1}^{D}\left(1 - \hat{P}_i\right), \quad \hat{\mathcal{P}}_1 = \sum\nolimits_{i=1}^{D} \hat{P}_i \underbrace{\Pi(1 - \hat{P}_j)}_{\substack{j=1,...,D \\ j \neq i}}, \quad \hat{\mathcal{P}}_2 = \sum\nolimits_{i=1}^{D-1}\sum\nolimits_{j=i+1}^{D} \hat{P}_i \hat{P}_j \underbrace{\Pi(1 - \hat{P}_n)}_{\substack{n=1,...,D \\ n \neq i,\, n \neq j}} \quad (28)$$

where $\hat{P}_i, i = 1, 2, ..., D$ is a set of the false alarm probability estimates, which is specified for any $q \in \{0, 1, ..., n_{sp}^{\max}\}$ according to the number of spiky Doppler bins d_{sp} as given below

$$\begin{cases} \text{for } d_{\mathrm{sp}} \in \{1, ..., D\}: \; \{\hat{P}_i = \hat{P}_{\mathrm{fa:1}}\left(n_{\mathrm{sp}}^{\max}\right), \; i = 1, ..., d_{\mathrm{sp}}, \; \hat{P}_i = P_{\mathrm{fa}}, \; i = d_{\mathrm{sp}} + 1, ..., D\} \\ \text{if } d_{\mathrm{sp}} = 0 \text{ or } n_{\mathrm{sp}}^{\max} = 0: \; \{\hat{P}_i = P_{\mathrm{fa}}, \; i = 1, ..., D\} \end{cases} \quad (29)$$

It should be noted that Eq. (29) assumes equal $\hat{P}_{\mathrm{fa:1}}(n_{\mathrm{sp}}^{\max})$ values for all spiky Doppler bins.

Table 1 summarizes the estimates $\hat{P}_{\mathrm{fa}}(n_{\mathrm{sp}}|1)$, $n_{\mathrm{sp}} = 0, 1, ..., n_{\mathrm{sp}}^{\max}$, $n_{\mathrm{sp}}^{\max} = Q - K_c + 1 = 7$. To obtain the estimates in Table 1, we performed 10^7 Monte-Carlos for each fixed n_{sp} value from the set $1, 2, ..., n_{\mathrm{sp}}^{\max}$; for $n_{\mathrm{sp}} = 0$, we use the nominal P_{fa} value $\hat{P}_{\mathrm{fa}}(0|1) = 10^{-3}$. Table 2 summarizes the estimates $\hat{P}_{\mathrm{fa:1}}(n_{sp}^{\max})$, $n_{sp}^{\max} = 0, 1, ..., 7$, computed from Eq. (26) using the corresponding data from Table 1.

Table 1. Estimates of conditional individual probability of false alarm $P_{\mathrm{fa}}(n_{\mathrm{sp}}|1)$.

NJD integration	Number of strong spikes per one Doppler bin n_{sp}							
method	0	1	2	3	4	5	6	7
FVI	10^{-3}	1	1	1	1	1	1	1
CVI	10^{-3}	3.6378×10^{-3}	12.5719×10^{-3}	40.6964×10^{-3}	11.9266×10^{-2}	30.6868×10^{-2}	6.46334×10^{-1}	1

To characterize the NJD-CVI' and NJD-FVI' robustness to the strong spikes, we use the overall probability of false alarm $P_{\mathrm{FA}}(n_{\mathrm{sp}}^{\max}|d_{\mathrm{sp}})$. We computed the estimates $\hat{P}_{\mathrm{FA}}(n_{\mathrm{sp}}^{\max}|d_{\mathrm{sp}})$, $n_{sp}^{\max} = 0, 1, ..., 7$, $d_{\mathrm{sp}} \in \{1, 2, ..., 5\}$ from Eqs. (27)–(29) using the corresponding data from Table 2.

Table 2. Estimates of unconditional individual probability of false alarm $P_{\mathrm{fa:1}}(n_{\mathrm{sp}}^{\max})$.

NJD integration	Maximum number of strong spikes $n_{\mathrm{sp}}^{\max}$ per one Doppler bin							
method	0	1	2	3	4	5	6	7
FVI	10^{-3}	0.5005000	0.6670000	0.7502500	0.8002000	0.8335000	0.8572857	0.8751250
CVI	10^{-3}	2.3189×10^{-3}	5.7366×10^{-3}	14.4765×10^{-3}	35.4345×10^{-3}	8.06735×10^{-2}	16.14821×10^{-2}	26.62968×10^{-2}

Figure 7 compares the detectors' robustness under the same settings that we used for Figure 5. The simulation has shown that the plots in Figure 7 computed for the spike-to-noise ratio SpNR $\geq 20\,\mathrm{dB}$ are almost indistinguishable from the corresponding plots obtained for infinitely strong spikes. Thus, this figure shows the results of the simulation for SpNR $=$ Inf only. These results present the worst-case increase in the individual and the overall probability of false alarm.

From Figure 7, it can be seen that NJD-CVI exhibits essentially enhanced robustness to the strong spikes relative to NJD-FVI. For these detectors, Table 3 compares the overall probability of false alarm using the estimates $\hat{P}_{\mathrm{FA}}(n_{sp}^{\max}|d_{\mathrm{sp}})$, $n_{sp}^{\max} = 1, 2, 3$ taken from Figure 7 for $d_{\mathrm{sp}} = 2, 3$. As one can see in Table 3, the values of $\hat{P}_{\mathrm{FA}}(1|2)$, $\hat{P}_{\mathrm{FA}}(2|2])$, and $\hat{P}_{\mathrm{FA}}(3|2)$ for NJD-CVI are lower than those for NJD-FVI by about four orders of magnitude. For $d_{\mathrm{sp}} = 3$, the advantage of NJD-CVI over NJD-FVI is even more essential. Indeed, the estimates $\hat{P}_{\mathrm{FA}}(1|3)$, $\hat{P}_{\mathrm{FA}}(2|3])$, and $\hat{P}_{\mathrm{FA}}(3|3)$ for NJD-CVI are lower than those for NJD-FVI by about 7, 6, and 5 orders of magnitude, respectively.
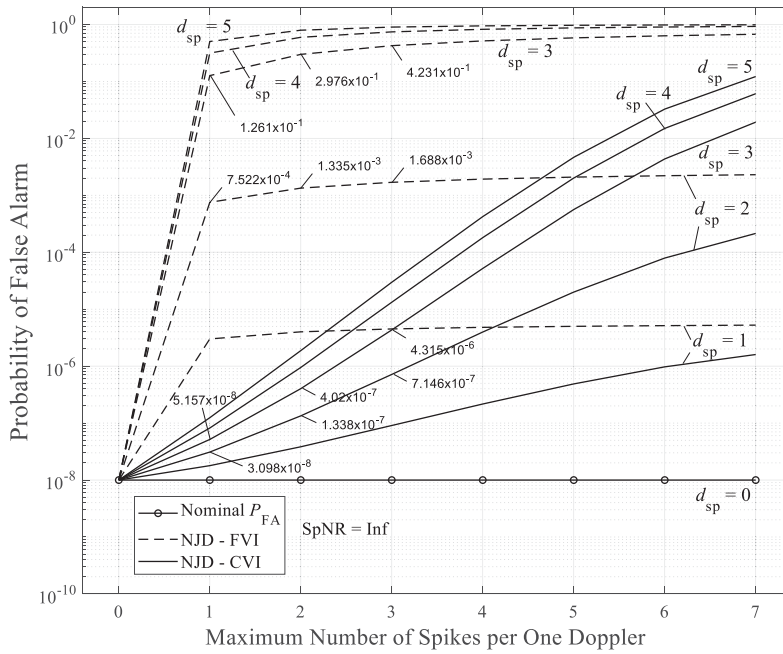
Figure 7. Comparison of false alarm performance for NJD-CVI and NJD-FVI detectors in the presence of strong spikes in CUT: Estimates of the overall probability of false alarm $P_{\mathrm{FA}}(n_{\mathrm{sp}}^{\mathrm{max}}|d_{\mathrm{sp}})$.

Table 3. Comparison of estimates of overall probability of false alarm $P_{\mathrm{FA}}(n_{sp}^{\mathrm{max}}|d_{\mathrm{sp}})$.

d_{sp}	NJD version	Maximum number of strong spikes n_{sp}^{max} per one Doppler bin			
		0	1	2	3
2	NJD-FVI	9.985×10^{-9}	7.522×10^{-4}	1.335×10^{-3}	1.688×10^{-3}
	NJD-CVI	9.985×10^{-9}	3.098×10^{-8}	1.338×10^{-7}	7.146×10^{-7}
3	NJD-FVI	9.985×10^{-9}	1.261×10^{-1}	2.976×10^{-1}	4.231×10^{-1}
	NJD-CVI	9.985×10^{-9}	5.157×10^{-8}	4.020×10^{-7}	4.315×10^{-6}

4. ADAPTIVE NOISE JAMMING DETECTOR

4.1. Block Diagram

This section addresses the noise jamming detection in situations where the receiver noise power σ_n^2 is *unknown*. In order to provide the CFAR property, the detection algorithm has to estimate the receiver noise power and adjust the detection threshold accordingly. We refer to this algorithm as the adaptive noise jamming detector (AJD).

Figure 8 shows a block diagram of an AJD with CVI (AJD-CVI) as a sequence of operations implemented by a primary set of computing units CU1, ..., CU5, and a secondary set of computing units CU6, CU7, and CU8. The primary computing units, except for CU4, perform operations identical to those of the corresponding CUs in NJD-CVI (see Figure 3). CU1 produces a set of vectors $\mathbf{v}_i$, $i = 1, ..., D$ as given by Eq. (7) for the k-th current antenna scan. CU2 generates the set of ordered samples $\mathbf{x}_i$, $i = 1, 2, ..., D$ as Eq. (8) gives. CU3 computes the scalar values Y_i $(i = 1, 2, ..., D)$ using CVI as given by Eq. (9). CU5 finalizes the noise jamming detection as given by Eq. (11).

In Figure 8, CU4 exploits an adaptive CFAR method (Appendix A describes this method in detail). CU4 carries out the following operations:
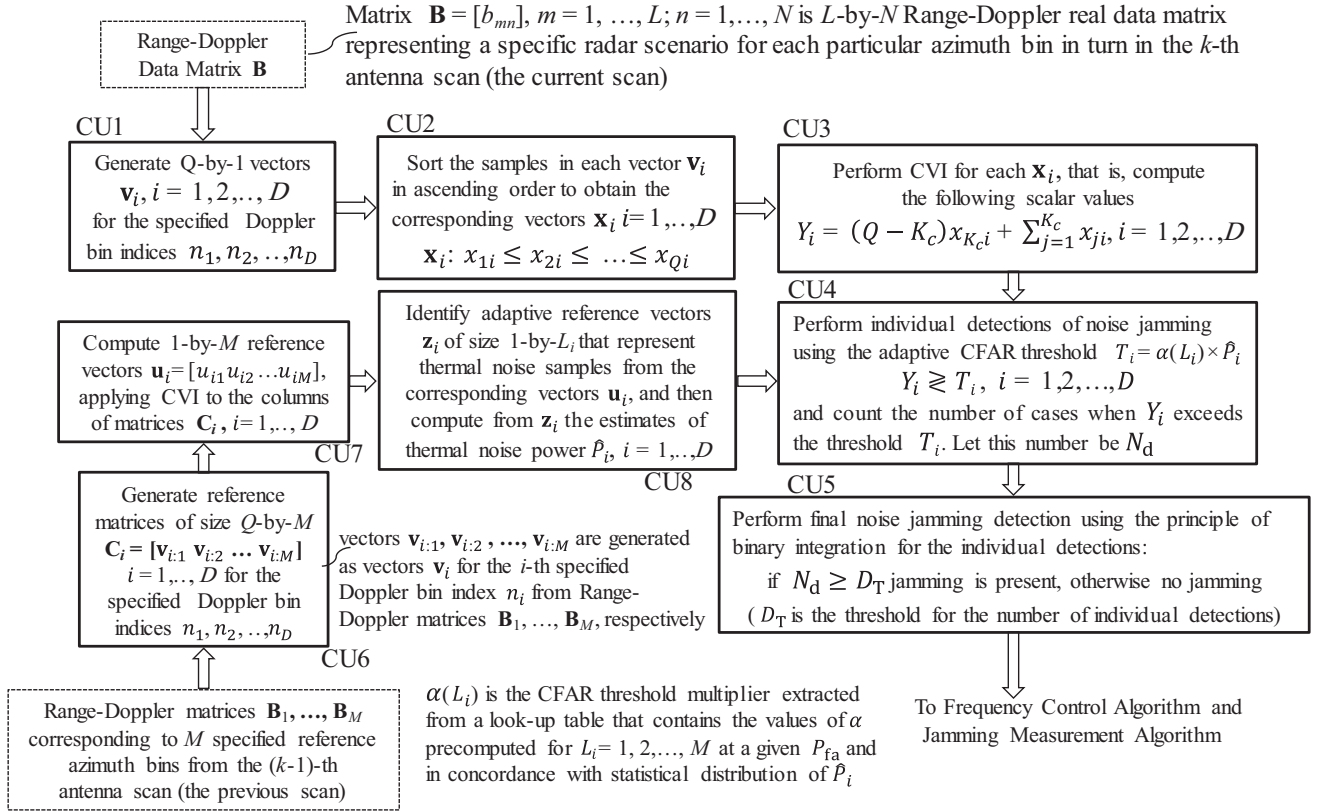
Matrix $\mathbf{B} = [b_{mn}]$, $m = 1, \ldots, L$; $n = 1, \ldots, N$ is L-by-N Range-Doppler real data matrix representing a specific radar scenario for each particular azimuth bin in turn in the k-th antenna scan (the current scan)

```
┌─────────────────────┐
│  Range-Doppler      │
│  Data Matrix B      │
└─────────────────────┘
```

CU1

Generate Q-by-1 vectors $\mathbf{v}_i$, $i = 1, 2, \ldots, D$ for the specified Doppler bin indices $n_1, n_2, \ldots, n_D$

CU2

Sort the samples in each vector $\mathbf{v}_i$ in ascending order to obtain the corresponding vectors $\mathbf{x}_i$ $i = 1, \ldots, D$

$\mathbf{x}_i$: $x_{1i} \leq x_{2i} \leq \ldots \leq x_{Qi}$

CU3

Perform CVI for each $\mathbf{x}_i$, that is, compute the following scalar values

$Y_i = (Q - K_c)x_{K_c i} + \sum_{j=1}^{K_c} x_{ji}$, $i = 1, 2, \ldots, D$

CU4

Perform individual detections of noise jamming using the adaptive CFAR threshold $T_i = \alpha(L_i) \times \hat{P}_i$

$Y_i \gtrless T_i$, $i = 1, 2, \ldots, D$

and count the number of cases when Y_i exceeds the threshold T_i. Let this number be N_d

Compute 1-by-M reference vectors $\mathbf{u}_i = [u_{i1} u_{i2} \ldots u_{iM}]$, applying CVI to the columns of matrices $\mathbf{C}_i$, $i = 1, \ldots, D$

CU7

Generate reference matrices of size Q-by-M $\mathbf{C}_i = [\mathbf{v}_{i:1} \ \mathbf{v}_{i:2} \ \ldots \ \mathbf{v}_{i:M}]$ $i = 1, \ldots, D$ for the specified Doppler bin indices $n_1, n_2, \ldots, n_D$

CU6

CU8

Identify adaptive reference vectors $\mathbf{z}_i$ of size 1-by-L_i that represent thermal noise samples from the corresponding vectors $\mathbf{u}_i$, and then compute from $\mathbf{z}_i$ the estimates of thermal noise power $\hat{P}_i$, $i = 1, \ldots, D$

vectors $\mathbf{v}_{i:1}, \mathbf{v}_{i:2}, \ldots, \mathbf{v}_{i:M}$ are generated as vectors $\mathbf{v}_i$ for the i-th specified Doppler bin index n_i from Range-Doppler matrices $\mathbf{B}_1, \ldots, \mathbf{B}_M$, respectively

CU5

Perform final noise jamming detection using the principle of binary integration for the individual detections:

if $N_d \geq D_T$ jamming is present, otherwise no jamming (D_T is the threshold for the number of individual detections)

```
┌──────────────────────────────┐
│  Range-Doppler matrices      │
│  B₁, ..., B_M                │
│  corresponding to M specified│
│  reference azimuth bins from │
│  the (k-1)-th antenna scan   │
│  (the previous scan)         │
└──────────────────────────────┘
```

$\alpha(L_i)$ is the CFAR threshold multiplier extracted from a look-up table that contains the values of α precomputed for $L_i = 1, 2, \ldots, M$ at a given P_{fa} and in concordance with statistical distribution of $\hat{P}_i$

To Frequency Control Algorithm and Jamming Measurement Algorithm

Figure 8. Adaptive jamming detector with CVI (unknown receiver noise power).

a) Perform individual detections for each of specified Doppler bins using the sequence of statistical hypothesis tests as given by

$$Y_i \underset{H_o}{\overset{H_1}{\gtrless}} T_i, \quad i = 1, 2, \ldots, D \tag{30}$$

In Eq. (30), the adaptive CFAR threshold T_i is computed as $T_i = \alpha_i \hat{P}_i$, where $\hat{P}_i$ is an estimate of the background power due to the thermal noise in the i-th specified Doppler bin and $\alpha_i = \alpha(L_i)$ is the threshold multiplier extracted from a stored look-up table. This table contains the values of the threshold multipliers α precomputed for the predefined false alarm probability P_{fa} (identical for all specified Doppler bins). The threshold multiplier is computed as a function of the length of the adaptive reference vector (window) L_i in concordance with a distribution of the estimate $\hat{P}_i$.

b) Count the number of detections N_d (the number of cases when Y_i, $i = 1, 2, \ldots, D$ exceeds the adaptive CFAR detection threshold T_i) out of the total number of possible detections D;

c) Accumulate the vector of detected Y_i samples: $[Y_{i_1}, Y_{i_2}, \ldots, Y_{i_{N_d}}]$, and the vector of the thermal noise power estimates $[\hat{P}_{i_1}, \hat{P}_{i_2}, \ldots, \hat{P}_{i_{N_d}}]$, where the integers $i_1, i_2, \ldots, i_{N_d}$ are the indices of those Doppler bins at which noise jamming detection occurred.

In the secondary set, CU6 generates the reference matrices of size Q-by-M

$$\mathbf{C}_i = \begin{bmatrix} \mathbf{v}_{i:1} & \mathbf{v}_{i:2} & \ldots & \mathbf{v}_{i:M} \end{bmatrix} = \begin{bmatrix} v_{1i:1} & v_{1i:2} & \ldots & v_{1i:M} \\ v_{2i:1} & v_{2i:2} & \ldots & v_{2i:M} \\ \ldots & \ldots & \ldots & \ldots \\ v_{Qi:1} & v_{Qi:2} & \ldots & v_{Qi:M} \end{bmatrix}, \quad i = 1, 2, \ldots, D \tag{31}$$

for the specified Doppler bin indices n_i, $i = 1, 2, \ldots, D$.

CU7 computes the vectors of reference samples (reference vectors) of size 1-by-M

$$\mathbf{u}_i = \begin{bmatrix} u_{i1} & u_{i2} & \ldots & u_{iM} \end{bmatrix}, \quad i = 1, 2, \ldots, D \tag{32}$$

using the sorting procedure (identical to that of CU2) and CVI (identical to that of CU3) in each column of the corresponding matrix $\mathbf{C}_i$.

CU8 implements the following operations:

a) Estimate the adaptive reference vector of size 1-by-L_i

$$\mathbf{z}_i = [\ z_{i1} \quad z_{i2} \quad \ldots \quad z_{iL_i}\ ], \quad i = 1, 2, ..., D, \tag{33}$$

which represents the thermal noise samples (clear region) in the corresponding vector $\mathbf{u}_i$.

b) Compute the thermal noise power estimates $\hat{P}_i$ in the i-th specified Doppler bin from the corresponding adaptive reference vector $\mathbf{z}_i$ $(i = 1, ..., D)$.

Figure 9 illustrates how the reference data matrices $\mathbf{C}_i$ in Eq. (31) and the corresponding reference vectors $\mathbf{u}_i$ in Eq. (32), $i = 1, 2, ..., D$, are generated from data matrices associated with the specified reference azimuth bins. The columns in the i-th matrix $\mathbf{C}_i$ are the vectors $\mathbf{v}_{i:1}$, $\mathbf{v}_{i:2}$, ..., $\mathbf{v}_{i:M}$ marked as gray rectangular in the real-valued Range-Doppler data matrices $\mathbf{B}_1$, $\mathbf{B}_2$, ..., $\mathbf{B}_M$ generated at the $(k-1)$-th scan (previous antenna scan). In Figure 9, the vectors $\mathbf{v}_{i:1}$, $\mathbf{v}_{i:2}$, ..., $\mathbf{v}_{i:M}$ are generated identically to vectors $\mathbf{v}_i$ (see Section 3.2) by extracting the samples at the predefined range cells in the corresponding Doppler bins n_i $(i = 1, 2, ..., D)$ from the matrices $\mathbf{B}_1$, $\mathbf{B}_2$, ..., $\mathbf{B}_M$, respectively. Figure 10 shows the correspondence between these matrices and the M reference azimuth cells, which indices are a_1, a_2, ..., a_M, respectively.
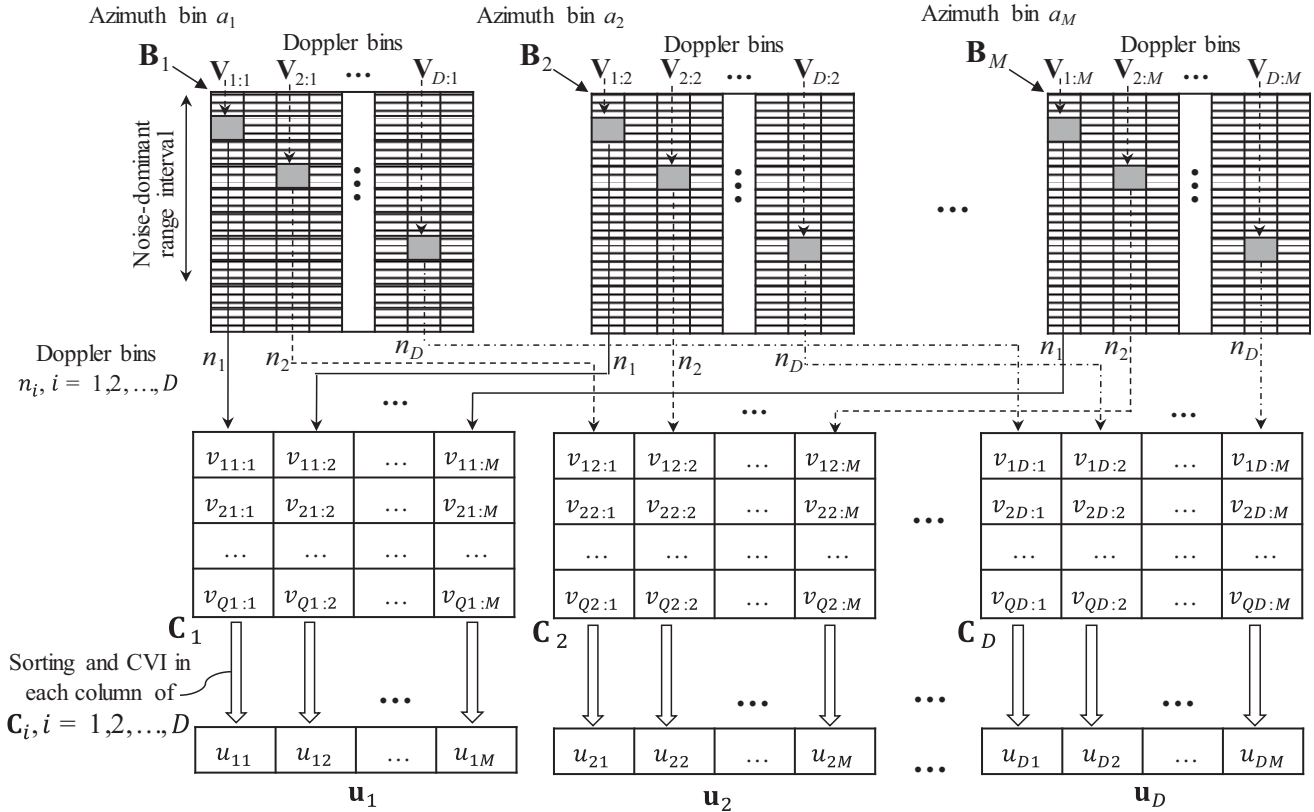
$\mathbf{u}_i = [u_{i1}, u_{i2}, ..., u_{iM}]$ are the 1-by-M vectors of reference samples for performing individual adaptive CFAR detection at the n_i-th Doppler bin, $i = 1, 2, ..., D$

Figure 9. Generating reference data matrices $\mathbf{C}_i$ and corresponding reference vectors $\mathbf{u}_i$.

Any possible spatial distribution for the reference azimuth bins is associated with the corresponding set of indices a_1, a_2, ..., a_M selected from a complete set of indices $[1, 2, ..., n_{az}]$, where n_{az} is the maximum index. For example, if the radar antenna scans within the azimuthal sector $\Delta\theta = 360°$ and the 3 dB antenna beamwidth is $\theta_3 = 1°$, then $n_{az} = \Delta\theta/\theta_3 = 360$.
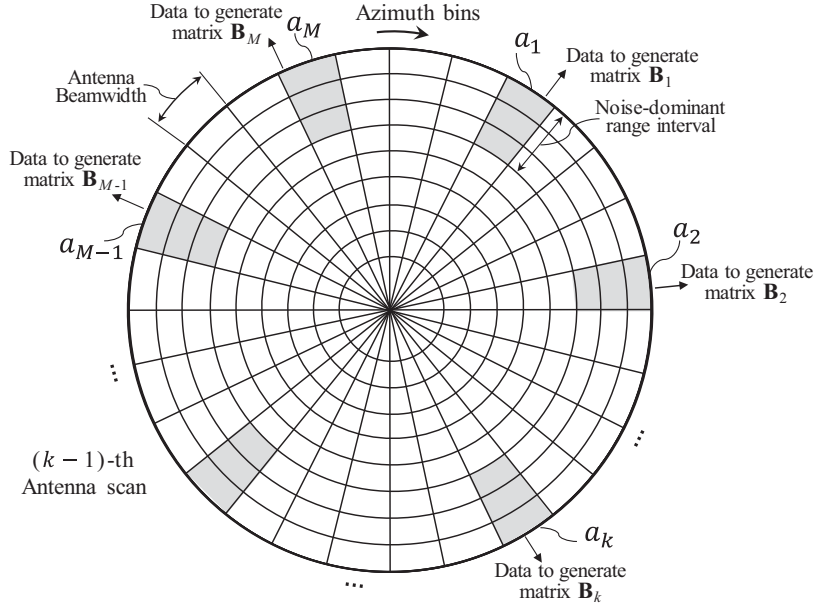
Figure 10. Range-Doppler data matrices $\mathbf{B}_i$ associated with reference azimuth bins a_i ($i = 1, ..., M$).

In selecting the distribution of reference azimuth bins for generating the matrices $\mathbf{B}_1$, $\mathbf{B}_2$, ..., $\mathbf{B}_M$, the primary criteria are to provide the mutual statistical independence between these matrices and minimize the number of reference bins simultaneously affected by interfering signals. To ensure statistical independence, we separate the selected azimuth bins as far as possible within the sector of angular scanning $\Delta\theta$. To avoid many "corrupted bins" due to noise jamming or strong spikes, we suggest equidistant distribution of reference azimuth bins within a given scanning sector $\Delta\theta$.

In generating a set of indices a_1, a_2, ..., a_M, one can use a deterministic approach (fixed set of indices from scan to scan) or a probabilistic approach (indices randomly change from scan to scan). Figure 11 illustrates both of these approaches.

Computing the 1-by-M reference vectors in Eq. (32) is the first step in adaptive CFAR processing. CU7 calculates the reference samples u_{i1}, u_{i2}, ..., u_{iM} in each $\mathbf{u}_i$, $i = 1, 2, ..., D$ by sequentially performing sorting and CVI for each column in the corresponding matrix $\mathbf{C}_i$ in Eq. (31) as given below by Eqs. (34)–(35).

$$\text{Sorting each column in } \mathbf{C}_i$$

$$\begin{cases} \mathbf{v}_{i:1} = [v_{1i:1}\ v_{2i:1}\ ...\ v_{Qi:1}]^T \rightarrow \mathbf{x}_{i:1} : x_{1i:1} \leq x_{2i:1} \leq ... \leq x_{Qi:1} \\ \mathbf{v}_{i:2} = [v_{1i:2}\ v_{2i:2}\ ...\ v_{Qi:2}]^T \rightarrow \mathbf{x}_{i:2} : x_{1i:2} \leq x_{2i:2} \leq ... \leq x_{Qi:2} \\ \mathbf{v}_{i:M} = [v_{1i:M}\ v_{2i:M}\ ...\ v_{Qi:M}]^T \rightarrow \mathbf{x}_{i:M} : x_{1i:M} \leq x_{2i:M} \leq ... \leq x_{Qi:M} \end{cases} \quad (34)$$

$$\text{Censored video integration (CVI)}$$

$$\begin{cases} u_{i1} = (Q - K_c)\, x_{K_c i:1} + \sum_{j=1}^{K_c} x_{ji:1} \\ u_{i2} = (Q - K_c)\, x_{K_c i:2} + \sum_{j=1}^{K_c} x_{ji:2} \\ u_{iM} = (Q - K_c)\, x_{K_c i:M} + \sum_{j=1}^{K_c} x_{ji:M} \\ \mathbf{u}_i = [u_{i1}\ u_{i2}\ ...\ u_{iM}] \end{cases} \quad (35)$$

The calculations according to Eqs. (34) and (35) are repeated for $i = 1, 2, ..., D$.

The individual CFAR detectors in Eq. (30) cannot directly use the reference samples from the corresponding reference vectors $\mathbf{u}_i$, $i = 1, 2, ..., D$ because these samples may be corrupted by noise jamming or other interfering signals. For example, assume that noise jamming is present in one of
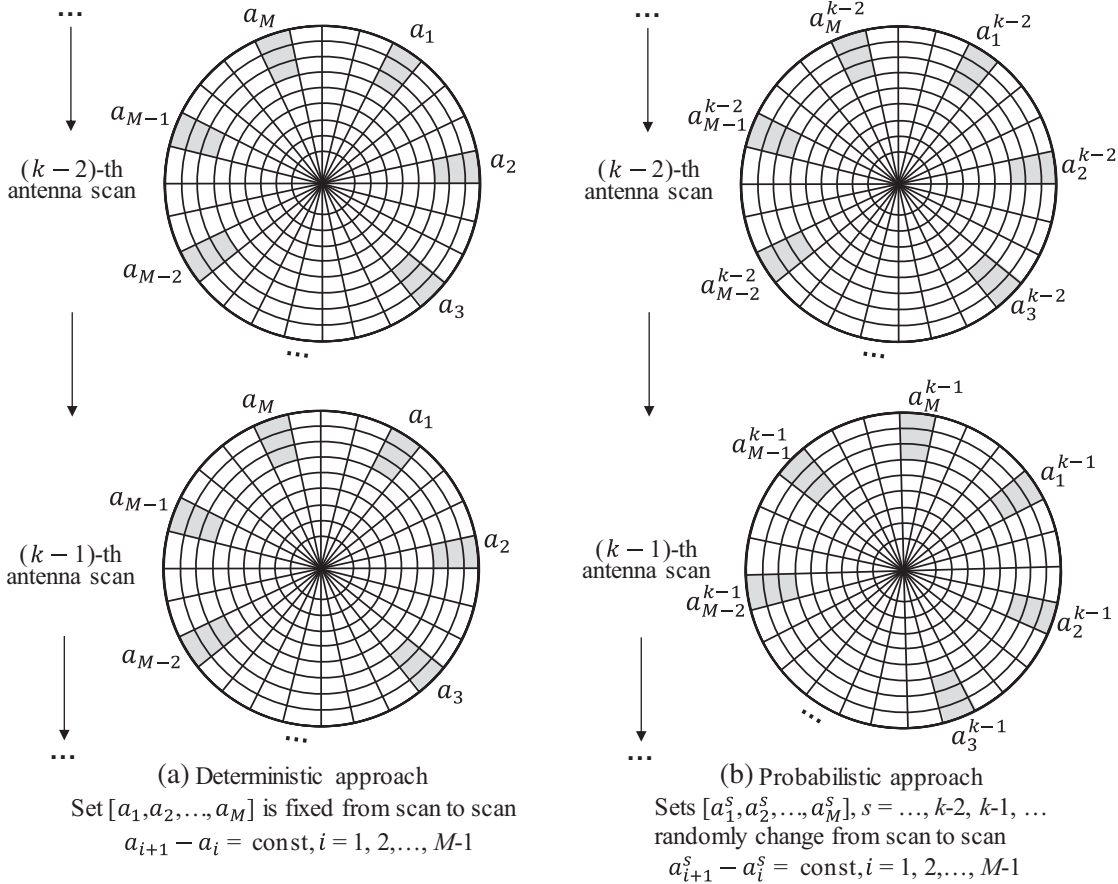
Figure 11. (a) Deterministic and (b) probabilistic approaches to generate reference azimuth bins.

the specified reference azimuth bins: let this bin index be a_1. Then all the samples in the associated Range-Doppler matrix $\mathbf{B}_1$ are corrupted by jamming, and, therefore, *all the samples* in the 1-st column (since the corrupted azimuth bin's index is a_1) of each matrix $\mathbf{C}_i$, $i = 1, 2, ..., D$ are corrupted as well (see Figure 9). After sorting and CVI according to Eqs. (34) and (35) *the first reference sample u_{i1} in each reference vector $\mathbf{u}_i$ will be corrupted* because the first K_c sorted samples included in the censored video integration remain affected by noise jamming even if the CVI-integrator discards the $Q - K_c$ largest samples.

The reference samples corrupted by jamming or other interfering signals are outliers since the average power of these samples may be significantly higher than that of the reference samples that represent the receiver thermal noise only. If strong outliers are present among the reference samples used in estimating the CFAR detection threshold, the threshold raises essentially. As a result, the individual probability of detection and the overall probability of detection degrades significantly.

To eliminate the detrimental effect of outliers on the CFAR detection performance, we propose an adaptive CFAR detection method that is a modification of the adaptive OFPI-CFAR (Outlier-Free Positions Identification CFAR) proposed in [12, 13]. To estimate an outlier-free CFAR threshold, this method identifies such an adaptive reference vector (or reference window), which is free of outliers. Using outlier-free adaptive reference windows eliminates the outliers' negative effect on the CFAR threshold and, finally, on the individual and overall detection performance. Appendix A describes the proposed adaptive CFAR technique in detail.

Whenever CU5 declares the presence of noise jamming, it sends an alarm signal to FCA (Frequency Control Algorithm) and the corresponding data to JMA (Jamming Measurement Algorithm) to select the best carrier frequencies for current radar operations.

4.2. AJD Performance Analysis

In this section, we analyze the AJD-CVI's performance using the same settings that have been used for the NJD detectors in Section 3: $P_{\text{fa}} = 10^{-3}$, $Q = 24$, $K = 18$, $D = 5$, $D_{\text{T}} = 3$. For the individual adaptive CFAR detector, we set the number of reference samples $M = 32$ and the probability of false censoring $P_{\text{fc}} = 10^{-4}$ (see the description of this detector in Appendix A). To identify an adaptive reference window of length $L \, (1 \leq L \leq M)$, this individual CFAR detector exploits the corresponding pairs of parameters R_m and β_m, $m = 1, 2, ..., M - 1$ for $P_{\text{fc}} = 10^{-4}$ from Table A1. In computing the detection threshold, the detector employs the optimum rank $K = \mathcal{K}(L)$ and the corresponding threshold multiplier $\alpha(L)$ for $P_{\text{fa}} = 10^{-3}$ from Table A2.

4.2.1. Detection Performance

A. With No Interference in Cell Under Test and Reference Data

We evaluate the detection performance of AJD-CVI using 10^5 Monte-Carlos. To estimate the overall probability of detection for AJD-CVI, we use Eq. (12), where an exact value of the individual probability of detection P_d is substituted with its estimate $\hat{P}_d$

$$\hat{P}_D = \hat{P}_D \left(D_T, D \right) = \sum_{k=D_T}^{D} \frac{D!}{k! \left(D - k \right)!} \hat{P}_d^k \left(1 - \hat{P}_d \right)^{D-k} \tag{36}$$

Figure 12 compares the overall receiver operating characteristic (ROC) of NJD-CVI and AJD-CVI, assuming no interference in all the reference azimuth bins. For NJD-CVI, we computed the theoretic ROC using Eqs. (19) and (12). As noted in Section 3, for a fixed "D_T-of-D" strategy at the final detection stage, NJD-CVI provides the ultimate detection performance for a given P_{FA} in no interference scenario. Therefore, no other detector can provide a higher overall probability of detection than NJD-CVI, other conditions being equal. In Figure 12, one can see that the ROC curve for AJD-CVI is pretty close to that for NJD-CVI. Indeed, AJD-CVI achieves the overall detection probability $P_D = 0.5$ at JNR $= -0.1459 \, \text{dB}$ that is just by 0.2 dB higher than the JNR $= -0.3442 \, \text{dB}$ required for NJD-CVI at the same P_D and P_{FA}.
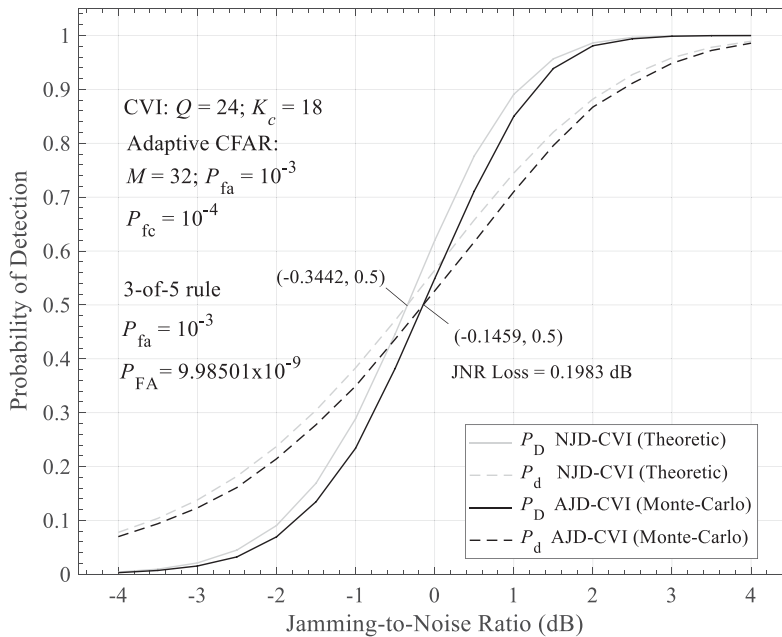

Figure 12. Comparison of overall ROC (P_D vs. JNR) for AJD-CVI and NJD-CVI.

B. In the Presence of Strong Spikes in CFAR Reference Data

This subsection analyzes the AJD-CVI's robustness regarding the overall probability of detection in the presence of strong spikes in CFAR reference data. First, we estimate the individual probability of detection P_d at a reference JNR in the presence of infinitely large spikes for the individual CFAR detector in Eq. (30). Figure 13 illustrates a possible scenario with strong spikes in the reference data matrix $\mathbf{C}_1$ associated with a single Doppler bin, which index is n_1 (see Figure 9). In this matrix, the j-th column ($j = 1, ..., M$) contains the Q-by-1 reference data vector $\mathbf{v}_{1:j}$ associated with the n_1-th Doppler bin in the real-valued Range-Doppler data matrix $\mathbf{B}_j$ associated with the j-th reference azimuth bins a_j. In this matrix, some columns may be corrupted by strong spikes.
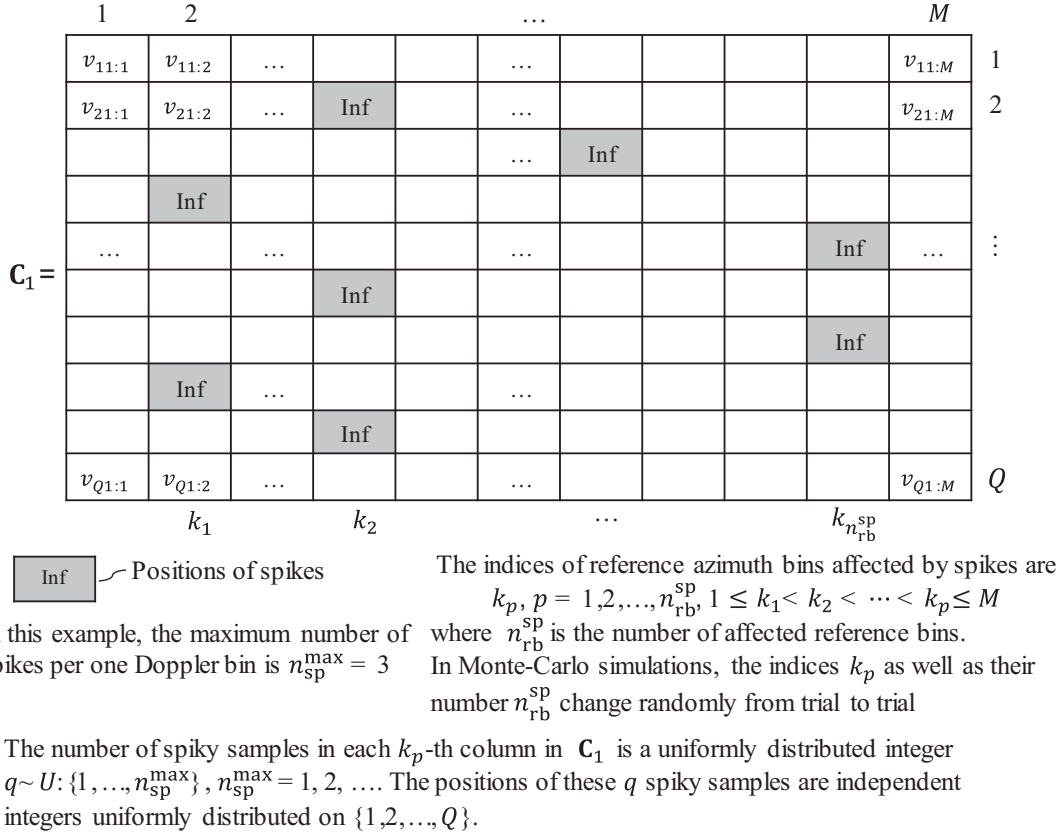
Figure 13. Spiky samples in reference data matrix for a single Doppler bin.

The number of spike-affected (spiky) azimuth bins in the entire scanning sector is assumed to be $n_{az}^{sp} = 36, 72, 108$: respectively, it makes up 10%, 20%, and 30% of the total number of the azimuth bins $n_{az} = 360$. For each fixed n_{az}^{sp} value, we generated a set of the spiky azimuth bins' indices as the first n_{az}^{sp} elements $j_1, j_2, ..., j_{n_{az}^{sp}}$ in a uniform random permutation of the set $\{1, 2, ..., n_{az}\}$.

We assumed that the number of spikes q in each spiky azimuth bin is a uniformly distributed integer $q \sim U : \{1, ..., n_{sp}^{max}\}$, where n_{sp}^{max} is the maximum number of spikes per one Doppler bin. The positions of these q spikes in the reference data vectors $\mathbf{v}_{1:j_r}$, $r = 1, 2, ..., n_{az}^{sp}$ associated with the spiky azimuth bins are q independent unique integers uniformly distributed on the set $\{1, 2, ..., Q\}$.

In the Monte-Carlo procedure for each fixed n_{az}^{sp}, the set of spiky azimuth bins is generated before the trials and then fixed during the simulation. The indices of the reference azimuth bins are simulated as a set of M random integers at each Monte-Carlo trial. The first reference azimuth bin's index a_1 is generated as an integer uniformly distributed on the set $\{10, 11, ..., 38\}$ and then a complete set of the reference azimuth bins $\{a_j, j = 1, ..., M\}$ is generated as $a_j = a_1 + 8(j - 1)$, $j = 1, ..., M$. The indices of spiky reference azimuth bins belong to the intersection of the set of spiky azimuth bins' indices

$\{j_1, j_2, ..., j_{n_{\text{az}}^{\text{sp}}}\}$ with the set of reference azimuth bins' indices $\{a_1, a_2, ..., a_M\}$. Hence, the indices of spiky reference azimuth bins k_p, $p = 1, 2, ..., n_{\text{rb}}^{\text{sp}}$, $1 \le k_1 < k_2 < ... < k_p \le M$ (see Figure 13) and their number $n_{\text{rb}}^{\text{sp}}$ change randomly from trial to trial. At each Monte-Carlo trial, the number of spiky samples q in the k_p-th column ($p = 1, ..., n_{\text{rb}}^{\text{sp}}$) in the matrix $\mathbf{C}_1$ is generated as the first element in a uniform random permutation of the set $\{1, ..., n_{\text{sp}}^{\text{max}}\}$. The positions of these q spiky samples are generated as the first q elements in a uniform random permutation of the set $\{1, 2, ..., Q\}$.

The reference jamming-to-noise ratio $\text{JNR}_o = 1.3659390$ was computed iteratively from Eq. (19) for the reference value of the individual probability of detection $P_{\text{do}} = 0.8$. This equation defines the P_d value for the individual detector in NJD-CVI. Using Eq. (12) yields the corresponding reference value of the overall detection probability $P_{\text{Do}} = 0.9420800$. For AJD-CVI, we obtained the corresponding reference individual probability of detection as $P_{\text{do}} = 0.7702845$ using linear interpolation at the point JNR_o for the AJD-CVI's data $P_d(\text{JNR})$ shown in Figure 12. From Eq. (12), the corresponding reference value of the overall probability of detection is $P_{\text{Do}} = 0.9167118$.

The result of the Monte-Carlo simulation is the estimates $\hat{P}_d$ of the individual probability of detection P_d conditioned on the number of spikes n_{sp} per one Doppler bin. Let these estimates be

$$\hat{P}_d (n_{\text{sp}}|1), \; n_{\text{sp}} = 0, 1, 2, ..., n_{\text{sp}}^{\text{max}} \tag{37}$$

where $n_{\text{sp}}^{\text{max}}$ is the maximal number of spikes per one Doppler bin; for $n_{\text{sp}} = 0$, we set $\hat{P}_d(0) = P_{\text{do}} = 0.7702845$. To compute the estimates of the unconditional individual probability of detection $\hat{P}_{d:1}(q)$, we use Eq. (26) after substituting the subscript "fa" with "d"

$$\hat{P}_{d:1}\left(n_{\text{sp}}^{\text{max}}\right) = \left(\frac{1}{q+1}\right) \sum\nolimits_{n_{\text{sp}}=0}^{q} \hat{P}_d (n_{\text{sp}}|1), \;\; q = 0, 1, ..., n_{\text{sp}}^{\text{max}} \tag{38}$$

Having obtained the estimates in Eq. (38), one can find the corresponding estimates of the overall probability of detection $P_D(n_{\text{sp}}^{\text{max}}|d_{\text{sp}})$ conditioned on the number of spiky Doppler bins $d_{\text{sp}} \in \{1, ..., D\}$ associated with CFAR reference data. We compute these estimates from Eqs. (27)–(29) where the subscripts "fa" and "FA" are substituted with "d" and "D," respectively. Thus, the estimates $\hat{P}_D(n_{\text{sp}}^{\text{max}}|d_{\text{sp}})$ are given by

$$\hat{P}_D(n_{\text{sp}}^{\text{max}}|d_{\text{sp}}) = 1 - \left[\hat{\mathcal{P}}_0 + \hat{\mathcal{P}}_1 + \hat{\mathcal{P}}_2\right]$$
$$d_{\text{sp}} \in \{1, ..., D\} \tag{39}$$

where $\hat{\mathcal{P}}_k$, $k \in \{0, 1, 2\}$, is the estimate of the probability of exactly k detections out of all D possible detections. Since the detections for different Doppler bins are mutually independent events, $\hat{\mathcal{P}}_k$ are given by

$$\hat{\mathcal{P}}_0 = \Pi_{i=1}^{D}\left(1 - \hat{P}_i\right), \quad \hat{\mathcal{P}}_1 = \sum\nolimits_{i=1}^{D} P_i \underbrace{\Pi(1 - \hat{P}_j)}_{\substack{j=1,...,D \\ j \neq i}}, \quad \hat{\mathcal{P}}_2 = \sum\nolimits_{i=1}^{D-1} \sum\nolimits_{j=i+1}^{D} \hat{P}_i \hat{P}_j \underbrace{\Pi(1 - \hat{P}_k)}_{\substack{k=1,...,D \\ k \neq i, k \neq j}} \tag{40}$$

where $\{\hat{P}_i, i = 1, ..., D\}$ is a set of the detection probability estimates defined as

$$\begin{cases} \text{for } d_{\text{sp}} \in \{1, ..., D\}: \{\hat{P}_i = \hat{P}_{d:1}(n_{\text{sp}}^{\text{max}}), i = 1, ..., d_{\text{sp}}, \hat{P}_i = P_{\text{do}}, i = d_{\text{sp}} + 1, ..., D\} \\ \text{if } d_{\text{sp}} = 0 \text{ or } n_{\text{sp}}^{\text{max}} = 0: \{\hat{P}_i = P_{\text{do}}, i = 1, ..., D\} \end{cases} \tag{41}$$

It should be noted that Eq. (41) assumes equal $\hat{P}_{d:1}(n_{\text{sp}}^{\text{max}})$ for all spiky Doppler bins.

Tables 4 and 5 respectively summarize the estimates $\hat{P}_d(n_{\text{sp}}|1)$ and $\hat{P}_{d:1}(n_{\text{sp}}^{\text{max}})$ for $n_{sp}^{\text{max}} = Q - K_c + 1 = 7$ in the scenario where $n_{\text{az}}^{\text{sp}} = 72$ spiky azimuth bins (20%) out of the total number of the azimuth bins $n_{\text{az}} = 360$ are affected by strong spikes. We obtained the former using 10^5 Monte-Carlo trials for each fixed n_{sp} value. For $n_{\text{sp}} = 0$, we set $\hat{P}_d(0|1) = P_{\text{do}} = 0.7702845$.

In Table 4, it can be seen that the estimates $\hat{P}_{\text{d}}(n_{\text{sp}}|1)$ gradually decrease when n_{sp} increases from 0 to 5: $\hat{P}_{\text{d}}(0|1) = 0.7703 > \hat{P}_{\text{d}}(1|1) > ... > \hat{P}_{\text{d}}(5|1) = 0.6372$. Then, $\hat{P}_{\text{d}}(6|1) = 0.6426$ becomes slightly

Table 4. Estimates of conditional individual probability of CFAR detection $P_d(n_{\text{sp}}|1)$.

Number of spikes n_{sp} per one Doppler bin							
0	1	2	3	4	5	6	7
0.7702845	0.7505750	0.7256000	0.6951100	0.6649350	0.6371500	0.6426100	0.7604500

Table 5. Estimates of unconditional individual probability of CFAR detection $P_{d:1}(n_{\text{sp}}^{\text{max}})$.

Maximum number of spikes $n_{\text{sp}}^{\text{max}}$ per one Doppler bin							
0	1	2	3	4	5	6	7
0.7702845	0.7604297	0.7488198	0.7353924	0.7213009	0.7072757	0.6980378	0.7058393

higher $\hat{P}_{\text{d}}(5|1)$, and, finally, one can see a relatively sharp increase from $\hat{P}_{\text{d}}(6|1)$ to $\hat{P}_{\text{d}}(7|1) = 0.7605$ that is fairly close to $\hat{P}_{\text{d}}(0|1) = P_{\text{do}} = 0.7703$.

This phenomenon relates to the following two factors. The first one is changing the statistical distributions of the elements in the reference vector (in our example, this is $\mathbf{u}_1$) after CVI (see Figure 9), depending on the number of strong spikes n_{sp} in spiky columns of the corresponding reference data matrix $\mathbf{C}_1$. The second one is changing the distributions of the corresponding adaptive detection threshold T_1 computed by adaptive CFAR detector using data extracted from the vector $\mathbf{u}_1$.

The adaptive CFAR detector (see Appendix A) applies the censoring procedure to the elements in vector $\mathbf{u}_1$, to discard outliers that appear due to interfering signals and identify an adaptive reference vector $\mathbf{z}_1$ of length $L_1 \in \{1, ..., M\}$. The elements in the vector $\mathbf{z}_1$ represent the receiver thermal noise. Using the adaptive reference vector $\mathbf{z}_1$, the adaptive CFAR detector computes the detection threshold $T_1 = \alpha(L_1)\hat{P}_1$, where α is the CFAR constant precomputed for a given P_{fa} as a function of L_1, and $\hat{P}_1$ is the receiver noise power estimate.

As shown in Subsection 3.3.2, in the presence of strong spikes in a data vector before CVI, the order statistics involved in CVI become statistically higher. Correspondingly, the output of CVI becomes statistically higher than that in the absence of strong spikes. Hence, for any spiky column in the reference data matrix $\mathbf{C}_1$ (see Figure 9), when n_{sp} gradually increases, some elements u_{1k} in the vector $\mathbf{u}_1 = [u_{11} \ u_{12} \ ... \ u_{1M}]$ become statistically higher accordingly. We refer to these as the corrupted elements. These are those u_{1k}, which indices k belong to a set of spiky reference azimuth bins, i.e., $k \in \{k_p, \ p = 1, 2, ..., n_{\text{rb}}^{\text{sp}}\}$, where $n_{\text{rb}}^{\text{sp}}$ is the number of reference bins corrupted by spikes. While n_{sp} increases from 1 to 5, the probability that significant corrupted elements appear in $\mathbf{u}_1$, also increases. However, they are not large enough to be discarded from $\mathbf{u}_1$ in the CFAR censoring procedure. Thus, the threshold T_1 increases and the individual (overall) probability of detection decreases accordingly. Nevertheless, when n_{sp} continues increasing from 6 to 7, at point $n_{\text{sp}} = 6$, the magnitudes of corrupted elements reach such a level that they are discarded with noticeably higher probability than that for $n_{\text{sp}} < 6$. Due to this discarding, the adaptive threshold T_1 decreases, and the individual and overall probability of detection increase somewhat. When $n_{\text{sp}} = Q - K_c + 1 = 7$, i.e., when n_{sp} exceeds $Q - K_c$, which is the CVI immunity threshold to the presence of strong spikes, then all the $n_{\text{rb}}^{\text{sp}}$ corrupted elements in $\mathbf{u}_1$ become infinitely strong. The CFAR censoring procedure discards all these corrupted elements from $\mathbf{u}_1$ with probability unity, and the adaptive reference vector $\mathbf{z}_1$ of length $L_1 = M - n_{\text{rb}}^{\text{sp}}$ represents only the thermal noise background. Hence, the adaptive detection threshold T_1 is not distorted by spikes since its level is determined by the receiver noise power estimated from the "clean" reference vector. Accordingly, the individual (overall) probability of detection increases noticeably relative to its value for $n_{\text{sp}} < 7$.

As one can see, the estimate $\hat{P}_{\text{d}}(7|1) = 0.7605(n_{\text{sp}} = 7)$ is slightly less than $P_{\text{do}} = 0.7703(n_{\text{sp}} = 0)$. This is because the average length $\bar{L}_1 = M - \overline{n_{rb}^{sp}}$ of the adaptive reference vector, where $\overline{n_{rb}^{sp}}$ is the average number of spiky reference azimuth bins, is slightly less than that $\bar{L}_1 = M$ for $n_{\text{sp}} = 0$. In scenarios with more dense spikes' distribution in azimuth, where $n_{\text{az}}^{\text{sp}}/n_{\text{az}} > 0.3$, the $\overline{n_{rb}^{sp}}$ increases and, accordingly, the

$\bar{L}_1$ decreases. This decrease in $\bar{L}_1$ results in a corresponding decreasing the individual/overall probability of detection for $n_{\mathrm{sp}} > Q - K_c$.

Figure 14 illustrates the phenomenon discussed above by comparing the conditional individual (a) and overall (b) probabilities of detection estimated using 10^5 Monte-Carlo trials. The ROC graphs in this figure were computed for $n_{\mathrm{sp}} = 4 < Q - K_c$ and $n_{\mathrm{sp}} = 7 > Q - K_c$ in a scenario with $n_{\mathrm{az}}^{\mathrm{sp}} = 108$ (30% of the total number of the azimuth bins).
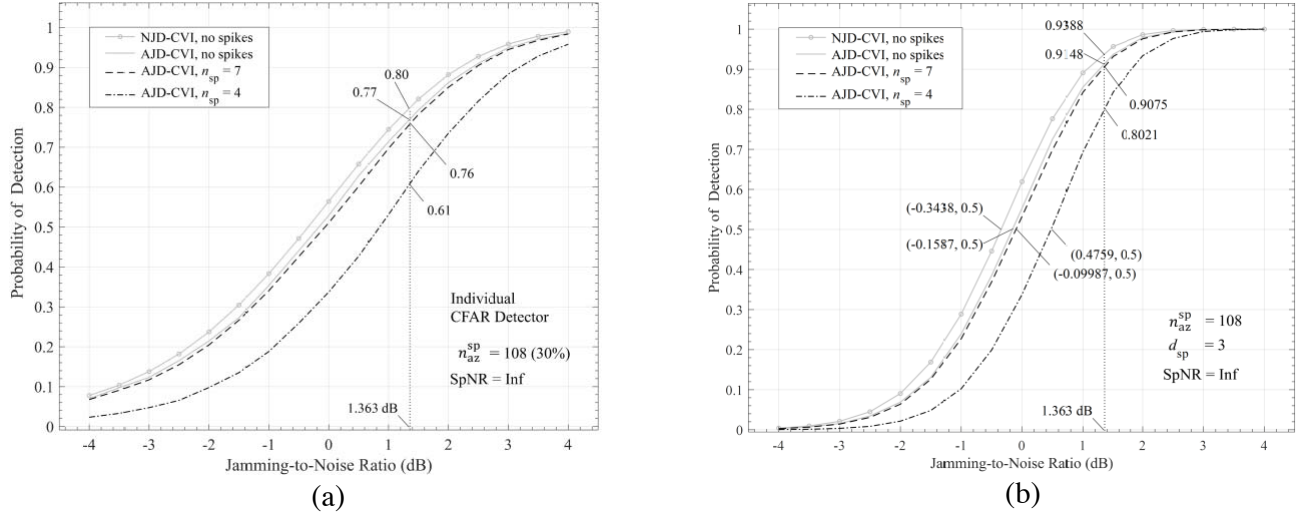
Figure 14. Effect of the number of spikes per one Doppler bin on the conditional probability of detection (a) individual probability $P_d(\mathrm{JNR}, n_{\mathrm{sp}}|1)$, (b) overall probability $P_D(\mathrm{JNR}, n_{\mathrm{sp}}|d_{\mathrm{sp}})$ for $d_{\mathrm{sp}} = 3$.

To characterize the robustness of the AJD-CVI's overall detection performance to the presence of strong spikes in the CFAR reference data, we use the estimates of the overall probability of detection $P_D(n_{\mathrm{sp}}^{\mathrm{max}}|d_{\mathrm{sp}})$, $n_{\mathrm{sp}}^{\mathrm{max}} = 0, 1, ..., 7$, conditioned on the number of spiky Doppler bins $d_{\mathrm{sp}} \in \{1, 2, ..., 5\}$. These estimates $\hat{P}_D(n_{\mathrm{sp}}^{\mathrm{max}}|d_{\mathrm{sp}})$ were computed from Eqs. (39)–(41) using the corresponding data in Table 5. Figure 15 shows the decrease in the overall probability of detection $P_D(n_{\mathrm{sp}}^{\mathrm{max}}|d_{\mathrm{sp}})$ relative to the reference value $P_{\mathrm{Do}} = 0.9167$ as a function of the maximum number of spikes $n_{\mathrm{sp}}^{\mathrm{max}}$ per one Doppler bin for a fixed number of spiky Doppler bins d_{sp}. This figure shows that as d_{sp} increases, the overall probability of detection decreases relative to P_{Do} for the scenario without interference in the CFAR reference data. For example, for $d_{\mathrm{sp}} = 3$ the maximum decrease in the probability takes place at $n_{\mathrm{sp}}^{\mathrm{max}} = 6$ and is about 5%: $(1 - 0.8715/0.9167) = 0.0493$. In the worst-case scenario, when $d_{\mathrm{sp}} = 5$, i.e., strong spikes are in all Doppler bins, the maximum decrease in the overall probability of detection does not exceed 10%: $(1 - 0.8343/0.9167) = 0.0899$.

Therefore, even in the worst-case situation ($d_{\mathrm{sp}} = 5$), the AJD-CVI's overall detection performance is highly robust to the presence of strong spikes in the CFAR reference data.

To show the effect of the number of spiky azimuth bins $n_{\mathrm{az}}^{\mathrm{sp}}$ on the overall probability of detection $P_D(n_{\mathrm{sp}}^{\mathrm{max}}|d_{\mathrm{sp}})$ conditioned on d_{sp}, Figure 16 compares the estimates $\hat{P}_D(n_{\mathrm{sp}}^{\mathrm{max}}|d_{\mathrm{sp}})$ for $n_{\mathrm{az}}^{\mathrm{sp}} = 36, 72$, and 108 (10, 20, and 30% of the total number of azimuth bins, respectively) at a fixed number of spiky Doppler bins ($d_{\mathrm{sp}} = 3$). This figure demonstrates that AJD-CVI provides reliable detection performance in dense spiky environments. Indeed, even when 30% of the total number of azimuth bins are affected by strong spikes ($n_{\mathrm{az}}^{\mathrm{sp}} = 108$), the minimal overall probability of detection is 0.8279 (at point $n_{\mathrm{sp}}^{\mathrm{max}} = 6$). Moreover, the overall detection probability loss less than 10%: $1 - 0.8279/0.9167 = 0.0969$.

Thus, the results shown in Figures 15 and 16 confirm that the AJD-CVI detector can maintain reliable noise jamming detection in the presence of strong spikes in the CFAR reference data.
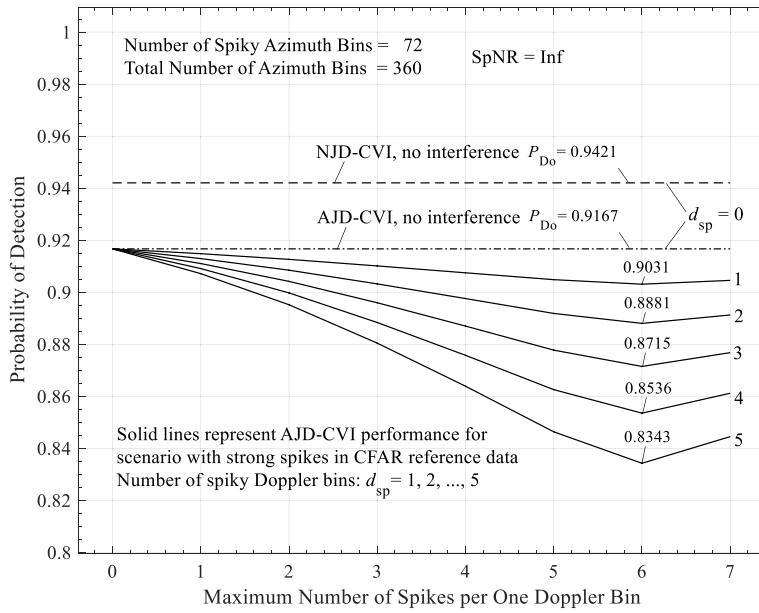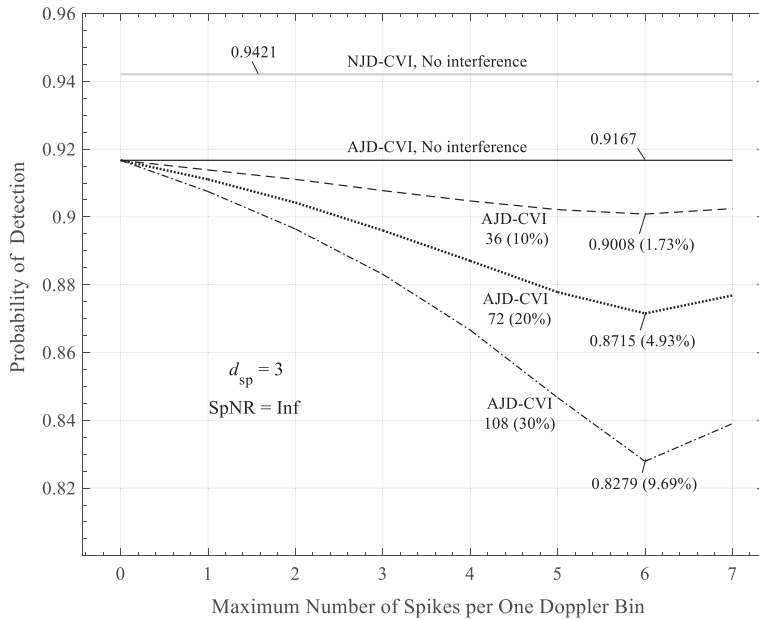
Figure 15. Robustness of AJD-CVI to the presence of strong spikes in CFAR reference data. Estimates of the overall probability of detection $P_D(n_{\mathrm{sp}}^{\max}|d_{\mathrm{sp}})$ versus the maximum number of spikes $n_{\mathrm{sp}}^{\max}$ per one Doppler bin at fixed number of spiky Doppler bins d_{sp}; the number of spiky azimuth bins $n_{\mathrm{az}}^{\mathrm{sp}} = 72$ (20% of the total number of azimuth bins n_{az}).

Figure 16. Robustness of AJD-CVI to the presence of strong spikes in CFAR reference data. Estimates of the overall probability of detection $P_D(n_{\mathrm{sp}}^{\max}|d_{\mathrm{sp}})$ for different number of spiky azimuth bins $n_{\mathrm{az}}^{\mathrm{sp}} = 36$, 72, and 108 at a fixed number of spiky Doppler bins ($d_{\mathrm{sp}} = 3$).

C. In the Presence of Noise Jamming in CFAR Reference Data

Figure 17 shows the robustness of the AJD-CVI's overall detection performance to the presence of noise jamming in the reference azimuth bins. The number of "jammed" azimuth bins $n_{\mathrm{az}}^{\mathrm{jam}}$, i.e., the
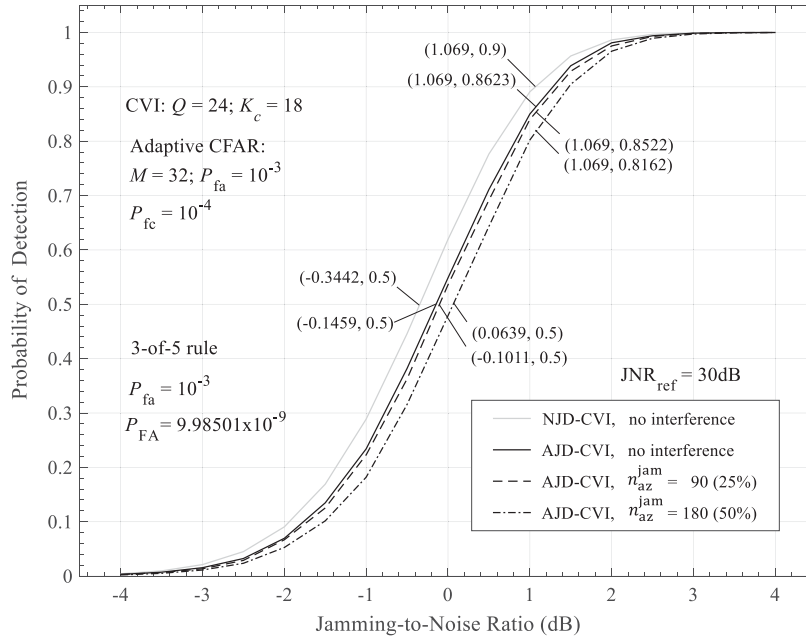
Figure 17. Robustness of the AJD-CVI's overall detection performance $P_D(\text{JNR}|D)$, $D = 5$, to the presence of noise jamming in CFAR reference data.

number of azimuth bins out of the total number of azimuth bins $n_{\text{az}} = 360$, is assumed to be $n_{\text{az}}^{\text{jam}} = 90$ and 180 (25 and 50% of n_{az}, respectively). In the Monte-Carlo trials for each fixed $n_{\text{az}}^{\text{jam}}$ value, the indices for jammed azimuth bins were generated before trials and then fixed during the simulations. The indices of jammed azimuth bins were generated as the first $n_{\text{az}}^{\text{jam}}$ elements from a uniform random permutation of the set $\{1, 2, ..., n_{\text{az}}\}$. The indices of the reference azimuth bins were generated as a random set of M integers at each independent trial as described in Subsection 4.2.1B. The estimates of the overall probability of detection $P_D(\text{JNR}|D)$ with $D = 5$ were computed using Eqs. (38)–(40) and modified Eq. (41) (see Subsection 4.2.1B). In the modified Eq. (41), we set $\hat{P}_i = \hat{P}_{d:1}(\text{JNR})$, $i = 1, ..., D$ at each JNR-value. This setting is used because even if one reference azimuth bin is corrupted by noise jamming, all reference vectors $\mathbf{u}_i$, $i = 1, ..., D$ associated with D specified Doppler bins contain jamming-corrupted samples. Indeed, if a noise jamming is present in the k-th reference azimuth bin a_k then *all* the samples in the associated Range-Doppler matrix $\mathbf{B}_k$ are corrupted by this jamming, and, therefore, *all* the samples in the k-th column of each matrix $\mathbf{C}_i$, $i = 1, 2, ..., D$ (see Figure 9) are corrupted as well. After sorting and CVI according to Eqs. (34) and (35), the k-th reference sample $\mathbf{u}_{ik}$ in each reference vector $\mathbf{u}_i$ will inevitably be corrupted by jamming. This is because the first K_c sorted samples remain affected by noise jamming even if the $Q - K_c$ largest samples are discarded before CVI. To compute the estimates of the conditional probability of detection $P_d(\text{JNR}|1)$, we used 10^5 Monte-Carlo trials for each JNR value. For the jamming in the reference data, we set the jamming-to-noise ratio $\text{JNR}_{ref} = 30$ dB.

Figure 17 shows that AJD-CVI is highly robust to the number of azimuth bins corrupted by jamming. This statement is valid even in the case of highly dense jamming distribution in azimuth. Indeed, even if 50% percent ($n_{\text{az}}^{\text{jam}} = 180$) of the total azimuth bins are jammed, the JNR loss (at point $P_D = 0.5$) is relatively small: 0.21 and 0.41 dB, respectively, relative to the JNR required for AJD-CVI and NJD-CVI in the case of no interference. Let us assume the P_D-values 0.9 and 0.8623 (at point JNR = 1.069 dB) are the reference values for NJD-CVI and AJD-CVI, respectively. As one can see, the loss in the overall probability of detection is also reasonably small: 9.31% ($1 - 0.8162/0.9 = 0.0931$) relative to NJD-CVI and 5.35% ($1 - 0.8162/0.8623 = 0.0535$) relative to AJD-CVI.

4.2.2. False Alarm Performance in the Presence of Strong Spikes in CUT

This section analyzes the false alarm performance of AJD-CVI in the presence of infinitely strong spikes in the cell under test (CUT) compared to that of NJD-CVI. In this analysis, we consider the estimates of the overall probability of false alarm $P_{\mathrm{FA}}(n_{\mathrm{sp}}^{\max}|d_{\mathrm{sp}})$ as a function of the maximum number of strong spikes per one Doppler bin $n_{\mathrm{sp}}^{\max}$ for a fixed number of spiky Doppler bins d_{sp}. To compute these estimates, we used the methodology that has been used for the NJD-CVI/FVI detectors in Subsection 3.3.2.

Table 6 summarizes the estimates of the conditional probability of false alarm $P_{\mathrm{fa}}(n_{\mathrm{sp}}|1)$, $n_{\mathrm{sp}} = 0, 1, ..., n_{\mathrm{sp}}^{\max}$, $n_{\mathrm{sp}}^{\max} = Q - K_c + 1 = 7$ for both detectors in question. These estimates were computed using 10^7 Monte-Carlos for each fixed value of $n_{\mathrm{sp}} \in \{1, ..., n_{\mathrm{sp}}^{\max}\}$; for $n_{\mathrm{sp}} = 0$, we use the nominal P_{fa} value $P_{\mathrm{fa}}(0|1) = 10^{-3}$. Table 7 summarizes the estimates of the unconditional probability of false alarm $P_{\mathrm{fa:1}}(n_{sp}^{\max})$, $n_{sp}^{\max} = 0, 1, ..., 7$, calculated from Eq. (26) using the corresponding data from Table 6. The

Table 6. Estimates of conditional individual probability of false alarm $P_{\mathrm{fa}}(n_{\mathrm{sp}}|1)$.

Method	Number of strong spikes per one Doppler bin n_{sp}							
	0	1	2	3	4	5	6	7
NJD-CVI	10^{-3}	3.75×10^{-3}	12.46×10^{-3}	39.39×10^{-3}	11.796×10^{-2}	30.954×10^{-2}	6.4480×10^{-1}	1
AJD-CVI	10^{-3}	3.49×10^{-3}	11.66×10^{-3}	35.75×10^{-3}	10.593×10^{-2}	28.237×10^{-2}	6.1315×10^{-1}	1

Table 7. Estimates of unconditional individual probability of false alarm $P_{\mathrm{fa:1}}(n_{\mathrm{sp}}^{\max})$.

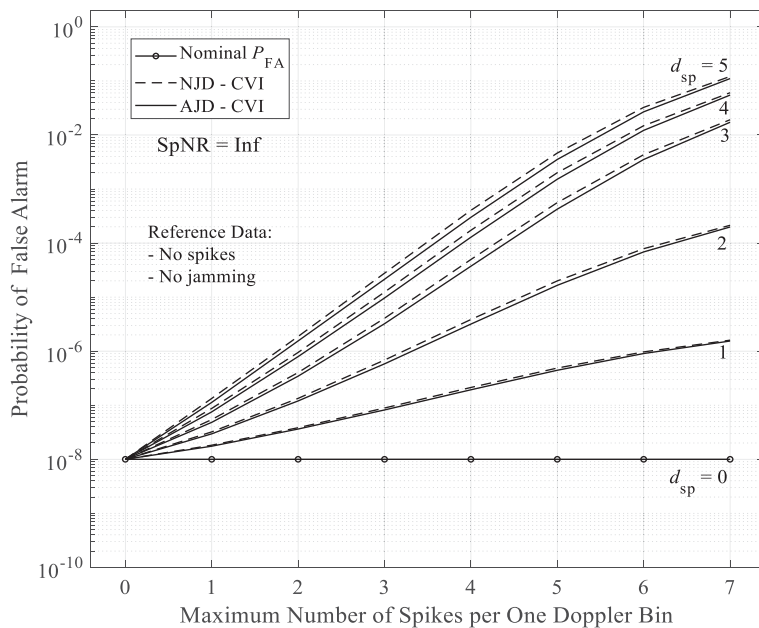| Method	Maximum number of strong spikes $n_{\mathrm{sp}}^{\max}$ per one Doppler bin							
	0	1	2	3	4	5	6	7
NJD-CVI	10^{-3}	2.3750×10^{-3}	5.7367×10^{-3}	14.150×10^{-3}	34.912×10^{-3}	8.0683×10^{-2}	1.61271×10^{-1}	2.66113×10^{-1}
AJD-CVI	10^{-3}	2.2450×10^{-3}	5.3833×10^{-3}	12.975×10^{-3}	31.566×10^{-3}	7.3367×10^{-3}	1.50478×10^{-1}	2.56669×10^{-1}

Figure 18. Comparison of AJD-CVI' and NJD-CVI' robustness using the estimates of the overall probability of false alarm $P_{\mathrm{FA}}(n_{\mathrm{sp}}^{\max}|d_{\mathrm{sp}})$, $d_{\mathrm{sp}} = 0, 1, ..., 5$, in the presence of strong spikes in CUT.

estimates $\hat{P}_{\text{FA}}(n_{\text{sp}}^{\max}|d_{\text{sp}})$, $n_{\text{sp}}^{\max} = 0, 1, ..., 7$, $d_{\text{sp}} \in \{1, 2, ..., D\}$ were obtained from Eqs. (27)–(29) using the corresponding data from Table 7.

Figure 18 shows that AJD-CVI is quite robust to strong spikes in the CUT and its robustness performance is essentially similar to that of NJD-CVI. As one can see, for each fixed d_{sp} value, the AJD-CVI curve goes slightly below the corresponding NJD-CVI curve. The reason for this is the well-known fact: the average CFAR detection threshold in the case of unknown noise power is somewhat higher than the fixed detection threshold in the case of known noise power. This is also the cause of the CFAR loss in the probability of detection relative to the fixed threshold detection.

5. CONCLUSION

This paper has introduced an adaptive CFAR method to detect continuous noise jamming in coherent radars with a single antenna having no pattern control. The proposed detector, called AJD-CVI, is designed under the condition that the receiver noise power is unknown. For noise jamming detection, the AJD-CVI detector uses data associated with a set of specified Doppler bins. These data are extracted from a real-valued Range-Doppler data matrix generated at the output of Doppler processing for each angular cell within the entire scanning sector. To mitigate the effect of sea, land, and weather clutter on detection performance, the proposed detector extracts the required data from a set of non-overlapping range intervals allocated within the noise-dominant region in the full range coverage.

In no interference scenario, the AJD-CVI detector ensures reliable noise jamming detection: its required JNR is pretty close to that of the non-adaptive detector, called NJD-CVI. The NJD-CVI detector assumes that the receiver noise power is known and provides the ultimate detection performance.

The AJD-CVI detector is also highly robust to interfering signals in the cell under test and CFAR reference data. The robustness is achieved by using a two-step detection algorithm. In the first step, the proposed detector removes interfering signals by performing censored video integration and individual adaptive CFAR detection in each of the specified Doppler bins. Then it applies the "m-of-n" detection strategy to a complete set of decisions declared by the individual CFAR detectors in the second step. This strategy provides immunity to the simultaneous presence of interfering signals in the data associated with the specified Doppler bins.

APPENDIX A. ADAPTIVE CFAR DETECTOR

In the present paper, we propose an adaptive CFAR detection method, a modification of the adaptive OFPI-CFAR (Outlier-Free Positions Identification CFAR) introduced in [12, 13]. To estimate an outlier-free CFAR threshold, our method identifies such an adaptive reference vector (or adaptive reference window), which is free of outliers due to noise jamming and other interfering signals. Using outlier-free adaptive reference windows eliminates the outliers' negative effect on the CFAR threshold and, finally, on the individual and overall detection performance.

We characterize the homogeneity of reference windows using the notions of the noise (clear) and interferer regions, which we denote by S_n and S_i, respectively. Figure A1 illustrates these regions using a sequence of sorted reference samples $x_{i1} \leq x_{i2} \leq ... \leq x_{iM}$ (assuming no samples intermixing between different regions) for the case when m noise-only samples and $M - m$ outliers are present in the reference vector $\mathbf{u}_i = [u_{i1}\ u_{i2}\ ...\ u_{iM}]$, $i \in \{1, 2, ..., D\}$, which is associated with this sequence. In a particular case, when no outliers are present in the reference vector $\mathbf{u}_i$, the clear region S_n completely characterizes the homogeneity of this vector because all M reference samples represent the receiver thermal noise.

Figure A2 shows a flowchart of an algorithm that the proposed adaptive CFAR method uses to identify an outlier-free (noise-only samples) adaptive reference vector (ARV). We refer to this algorithm as the ARV estimation algorithm. As can be seen, the ARV algorithm operates on the ordered sequence of the reference samples $x_{i1} \leq x_{i2} \leq ... \leq x_{iM}$ that is the result of sorting procedure performed for the i-th reference vector $\mathbf{u}_i = [u_{i1}\ u_{i2}\ ...\ u_{iM}]$, $i = 1, 2, ..., D$. The ARV algorithm estimates the total number of outlier-free samples L_i in the i-th reference vector $\mathbf{u}_i$ using the following step-by-step censoring procedure that is a modified version of the (r, q)-estimation algorithm from [12].
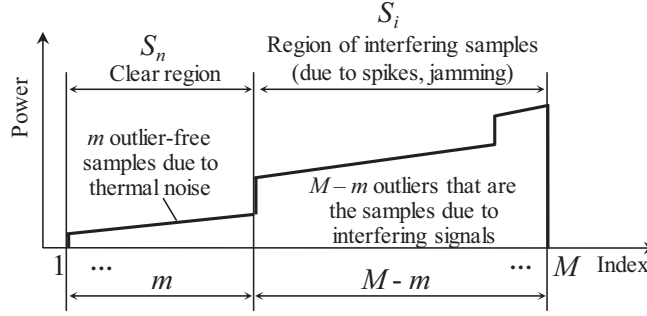
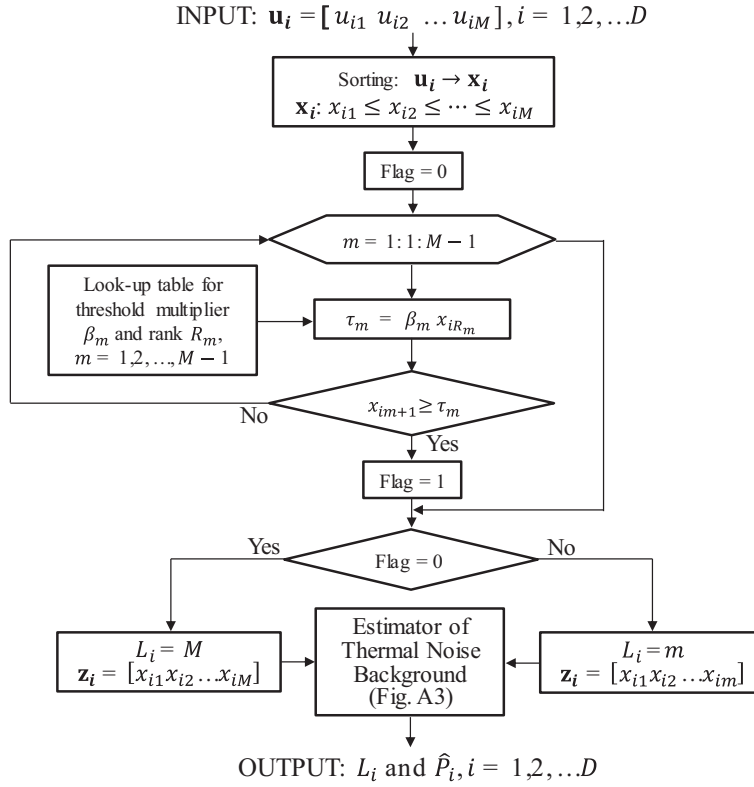**Figure A1.** Homogeneity regions in a reference window.

Figure A2. Estimator of adaptive reference window (ARV algorithm).

At the m-th step of the censoring procedure, $m = 1, 2, ..., M - 1$, the $(m + 1)$-th order sample x_{im+1} is compared against the censoring threshold $\tau_m = \beta_m x_{iR_m}$, where β_m is the censoring threshold multiplier at the m-th step, x_{iR_m} is the R_m-th sample selected from the current censoring window $x_{i1}, x_{i2}, ..., x_{im+1}$, and R_m is the representative sample rank at the m-th step. If for the first $m - 1$ steps, the adaptive censoring thresholds $\tau_j = \beta_j x_{iR_j}$, $j = 1, 2, ..., m - 1$ have not been exceeded and at the m-th step $x_{im+1} \geq \tau_m = \beta_m x_{iR_m}$ then the current step index m is the estimate of the total number of outlier-free reference samples, i.e., $L_i = m$. It is clear that $L_i = M$ when the procedure reaches the last step, i.e., $m = M - 1$ and $x_{iM} < \tau_{M-1}$.

For each reference vector $\mathbf{u}_i$ $(i = 1, ..., D)$, once the number of outlier-free reference samples L_i is estimated, the adaptive reference vector $\mathbf{z}_i = [z_{ij}| \ j = 1, ..., L_i]$ is readily identified as

$$\mathbf{z}_i = [x_{i1} \ x_{i2} \ ... \ x_{iL_i}], \ \ i = 1, 2, ..., D \tag{A1}$$

In [12], the censoring threshold multipliers β_m, $m = 1, 2, ..., M - 1$ are precomputed as OS-CFAR constants for the predetermined probability of false censoring P_{fc} and corresponding values of R_m

assuming homogeneous censoring reference window with exactly $m + 1$ samples, i.e., assuming that the outliers are infinitely strong and x_{im+1} is the last outlier-free sample. This assumption has also been used in [14] for deriving the censoring threshold multipliers based on the CA-CFAR principle. The values of R_m, $m = 1, 2, ..., M - 1$, are specified based on the optimum representative rank corresponding to the average decision threshold minimum [15]. We use the numerical procedure from [12] to compute the values of R_m and the corresponding values of β_m. Table A1 summarizes the results of this computation for $M = 32$, $P_{\mathrm{fc}} = 10^{-3}$ and 10^{-4}.

An estimate $\hat{P}_i$ of the average noise background level in the outlier-free region (clear region) at the i-th specified Doppler bin n_i $(i = 1, 2, ..., D)$ is required to compute the corresponding adaptive CFAR threshold T_i. In Figure 8, CU8 derives the estimate $\hat{P}_i$ from the corresponding adaptive reference
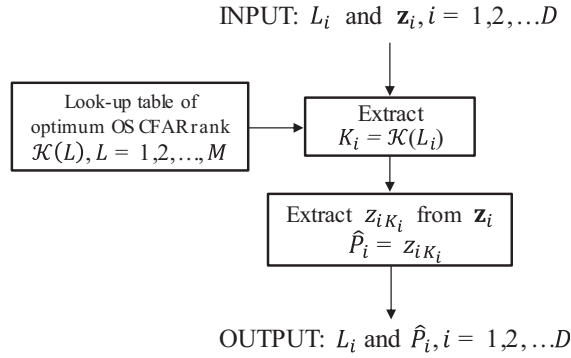

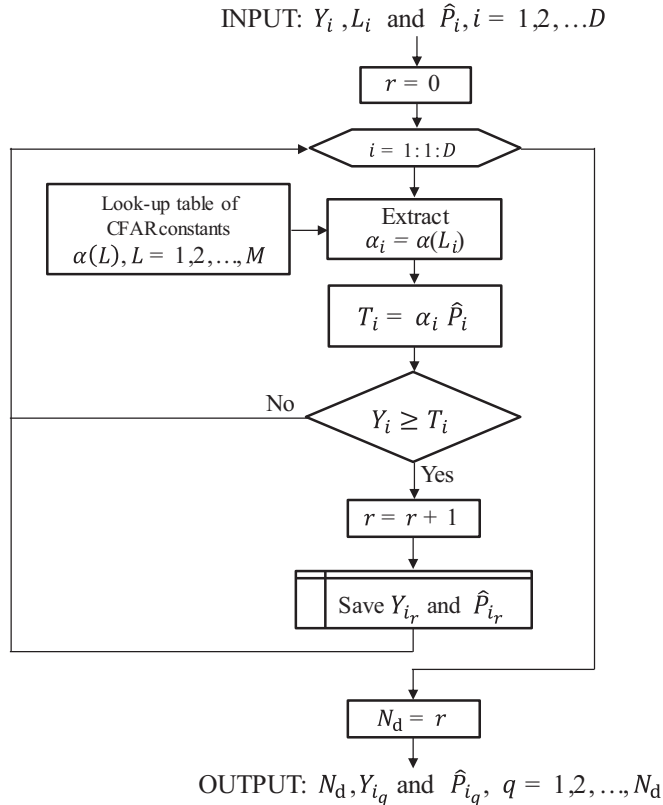**Figure A3.** Estimator of average noise background power.

Figure A4. Jamming detection using individual adaptive CFAR detectors.

Table A1. Optimum values of R_m and corresponding constant β_m for censoring procedure, $M = 32$.

m		P_{fc}		
		10^{-3}		10^{-4}
	R	β	R	β
1	1	4.390232	1	3.186795
2	2	3.085648	2	2.428126
3	3	2.700861	3	2.184419
4	4	2.509522	4	2.058686
5	5	2.392044	4	2.208169
6	5	2.539891	5	2.118923
7	6	2.450900	6	2.055927
8	6	2.550689	6	2.148828
9	7	2.480191	7	2.097261
10	7	2.556783	7	2.168103
11	8	2.498772	8	2.124682
12	9	2.451407	8	2.182259
13	9	2.512172	9	2.144845
14	10	2.470928	10	2.113296
15	10	2.522627	10	2.160646
16	11	2.486146	11	2.132394
17	12	2.454389	11	2.173573
18	12	2.498533	12	2.148011
19	13	2.469688	13	2.125398
20	13	2.508939	13	2.161150
21	14	2.482526	14	2.140282
22	14	2.517889	14	2.172449
23	15	2.493536	15	2.153081
24	16	2.471429	15	2.182332
25	16	2.503142	16	2.164267
26	17	2.482493	17	2.147734
27	17	2.511642	17	2.174173
28	18	2.492272	18	2.158592
29	18	2.519250	18	2.183043
30	19	2.501012	19	2.168311
31	20	2.484076	19	2.191060

Table A2. Optimum values of $K = \mathcal{K}(L)$ and corresponding OSCFAR constants $\alpha = \alpha(L)$ for adaptive CFAR detection, $M = 32$.

L		P_{fa}		
		10^{-3}		10^{-4}
	K	α	K	α
1	1	12.98819	1	11.61079
2	2	6.443261	2	5.985644
3	3	5.041953	3	4.739017
4	4	4.429446	4	4.186532
5	4	4.600121	4	4.353661
6	5	4.241963	5	4.027648
7	6	4.006293	6	3.811728
8	6	4.117032	6	3.920290
9	7	3.944968	7	3.761654
10	7	4.031351	7	3.846193
11	8	3.898141	8	3.722853
12	9	3.792067	9	3.624504
13	9	3.862233	9	3.693009
14	10	3.774298	10	3.611080
15	10	3.834424	10	3.669867
16	11	3.759745	11	3.599715
17	12	3.694565	12	3.537767
18	13	3.635798	13	3.481979
19	14	3.582717	14	3.432431
20	14	3.635235	14	3.482892
21	15	3.586587	15	3.437819
22	15	3.633653	15	3.482687
23	16	3.588950	16	3.441654
24	16	3.631418	16	3.481801
25	17	3.590359	17	3.444500
26	17	3.628813	17	3.480552
27	18	3.591197	18	3.446739
28	18	3.626060	18	3.479174
29	19	3.591735	18	3.511052
30	19	3.623341	19	3.477838
31	20	3.592160	19	3.506809
32	20	3.620794	20	3.476663

vector $\mathbf{z}_i$. Figure A3 is a block diagram of an estimator for computing the estimate $\hat{P}_i$ based on the OS-CFAR principle [12]. To compute $\hat{P}_i$, the procedure extracts from a stored look-up table the precomputed value of the representative CFAR rank K_i corresponding to the length L_i $(1 \leq L_i \leq M)$ of the adaptive reference vector $\mathbf{z}_i = [z_{i1} \ z_{i2} \ ... \ z_{iK_i} \ ... \ z_{iL_i}]$ and extracts the K_i-th ordered sample z_{iK_i} from this vector. As known from the OS-CFAR theory [15, 16], this sample z_{iK_i} can be treated as an

estimate of the background power, i.e., $\hat{P}_i = z_{iK_i}$, under the assumption that the reference window (vector) is homogeneous. For the proposed adaptive CFAR method, the optimum representative CFAR rank K is precomputed for each possible length $L \in \{1, 2, ..., M\}$ of the adaptive reference vector as such an integer that minimizes the average decision threshold (ADT) [15]. For each L, the optimum rank $K = \mathcal{K}(L)$ and the corresponding CFAR constant $\alpha(L)$ are computed as described in [12]. Table A2 summarizes the results for $M = 32$ at $P_\text{fa} = 10^{-3}$ and 10^{-4}.

Figure A4 shows a block diagram of the individual detectors (CU4 in Figure 8) based on the proposed adaptive CFAR method. The adaptive detection threshold T_i is a product $T_i = \alpha_i \hat{P}_i$, where $\alpha_i = \alpha(L_i)$ is extracted from a stored look-up table (Table A2 is an example). This table contains the values of α precomputed for a given P_fa in concordance with the statistical distribution of the receiver noise power estimate $\hat{P}_i = z_{iK_i}$ as a function of L $(L = 1, 2, ..., M)$.

REFERENCES

1. Melvin, W. L. and J. A. Scheer, *Principles of Modern Radars — Vol. II, Advanced Techniques*, Chapters 9 and 12, SciTech, Edison, NJ, USA, 2013.
2. Orlando, D., "A novel noise jamming detection algorithm for radar applications," *IEEE Signal Processing Letters*, Vol. 24, No. 2, 206–210, February 2017.
3. Cui, G., A. DeMaio, A. Aubry, A. Farina, and L. Kong, "Advanced SLB architectures with invariant receivers," *IEEE Transactions on Aerospace and Electronic Systems*, Vol. 49, No. 2, 798–818, April 2013.
4. Bandiera, F., A. Farina, D. Orlando, and G. Ricci, "Detection algorithms to discriminate between radar targets and ECM signals," *IEEE Transactions on Signal Processing*, Vol. 58, No. 12, 5984–5993, December 2010.
5. Li, K.-I, "Jamming detector and jamming detecting method," US Patent 7,835,687, 2010.
6. Kononov, A., J. H. Kim, and Y. C. Shin, "Noise jamming detection algorithm," *Proc. IEEE Radar Conf. RadarCon 2013*, Ottawa, ON, Canada, April 29–May 3, 2013.
7. Richards, M. A., *Fundamentals of Radar Signal Processing*, McGraw-Hill, New York, 2005.
8. Levanon, N., "Censored video integration in radar detection," *Proc. IEEE International Radar Conference*, Arlington, Virginia, May 7–10, 511–513, 1990.
9. Levanon, N., "Analytic comparison of four robust algorithms for post-detection integration," *IEE Proceedings — F*, Vol. 139, No. 1, 67–72, 1992.
10. Epstein, B. and M. Sobel, "Life testing," *Journal of the American Statistical Association*, Vol. 48, No. 263, 486–502, 1953.
11. Ritcey, J. A., "Performance analysis of the censored mean-level detectors," *IEEE Transactions on Aerospace and Electronic Systems*, Vol. 22, No. 4, 443–454, July 1986.
12. Kononov, A. A., J.-H. Kim, J.-K. Kim, and G. Kim, "A new class of adaptive CFAR methods for nonhomogeneous environments," *Progress In Electromagnetics Research B*, Vol. 64, 145–170, 2015.
13. Kononov, A. A., D. Kim, and H. S. Kim, "Adaptive CFAR method for nonhomogeneous environments and system thereof," Korean Patent 10-1871874, June 21, 2018.
14. Himonas, S. D. and M. Barkat, "Automatic censored CFAR detection for nonhomogeneous environments," *IEEE Transactions on Aerospace and Electronic Systems*, Vol. 28, No. 1, 286–304, January 1992.
15. Rohling, H., "Radar CFAR thresholding in clutter and multiple target situations," *IEEE Transactions on Aerospace and Electronic Systems*, Vol. 19, No. 4, 608–621, July 1983.
16. Shor, M. and N. Levanon, "Performance of order statistics CFAR," *IEEE Transactions on Aerospace and Electronic Systems*, Vol. 27, No. 2, 214–224, March 1991.